Multibody approach for reactive transport modeling in discontinuous-heterogeneous porous media

Adrien Socié, Frédéric Dubois, Yann Monerie, Frédéric Perales

Multibody approach for reactive transport modeling in discontinuous-heterogeneous porous media

Adrien Socié[1,2] · Frédéric Dubois[2,3] · Yann Monerie[2,3] · Frédéric Perales[1,2]

Abstract

In the context of long-term degradation of porous media, the coupling between fracture mechanics and reactive transport is investigated. A reactive transport model in a cracked discontinuous and heterogeneous porous medium is proposed. The species transport through and along the crack network are taken into account in a multibody approach. A dedicated geochemistry solver is developed and allows to take into account a significant number of chemical reactions. The model is validated via a benchmark for a porous medium without discontinuity. The applications deal with two kinds of chemical attacks in a pre-cracked concrete sample and highlight the impact of the discontinuities in the reactive transport kinetic and on the localization of the chemical degradation. The results bring out that a unidirectional descriptor, such as the depth of ingress rate, is not sufficient to describe the material degradation correctly.

Keywords Reactive transport · Cracked porous media · Geochemistry · Zero-thickness interface · Multibody approach

1 Introduction

In the context of the lifetime extension of nuclear structures and nuclear waste management, the French "Institut de Radioprotection et de Sûreté Nucléaire" (IRSN) leads research on the aging of geomaterials, such as cementitious materials [28]. Previous work dealt with chemo-thermo-mechanics and hydro-mechanics inducing delayed deformation of the matrix and cracking of the aggregates-matrix interface by differential deformation [4, 5, 12, 28]. In the case of long-term degradations, some studies focus on cracks description and numerical tools

✉ Frédéric Perales
  frederic.perales@irsn.fr

  Frédéric Dubois
  frederic.dubois@umontpellier.fr

  Yann Monerie
  yann.monerie@umontpellier.fr

[1] Institut de Radioprotection et de Sûreté Nucléaire,
    B.P. 3, 13115 Saint-Paul-lez-Durance Cedex, France

[2] MIST Laboratory, IRSN-CNRS-UM,
    Saint-Paul-lez-Durance Cedex, France

[3] LMGC, CNRS, Univ Montpellier, Montpellier, France

to accurately estimate the crack width [4, 12, 45, 59]. During chemistry attack such as external sulfate attack [19], chloride attack [13, 38], calcium leaching [17, 46] or delayed ettringite formation [29], cracks are preferred locii for ions diffusion and may accelerate the geomaterial degradation. These chemical degradations can affect the material properties and can have a significant impact on structural integrity. The present work focuses on the impact of cracks on chemical degradations in discontinuous-heterogeneous porous media.

As previously reported by several authors, the cracks have to be taken into account in transport simulations to improve the prediction of chemical attacks [19, 29, 38, 53]. Flow and species transport phenomena modeling in cracked porous media have been thoroughly studied in geomaterial aging such as hydro-fractured rocks [42, 57] or chemical attacks in soil and concrete [13, 38]. Two main approaches can be distinguished:

1. Mean diffusion modeling: the discontinuous porous medium is considered as an homogeneous medium where species diffusion through the discontinuity is not explicitly described but is taken into account with an effective diffusion coefficient. This diffusion coefficient varies with the crack density [22, 53], the use of double porosity approach [11] or the local damage value [38]. This kind of approach does not induce massive

numerical developments but failed in catching the localization effects due to the discontinuity.

2. Full field modeling: the geometry of the cracked medium is described. Two main strategies can be used: i) meshing the discontinuities to consider the different flows inside the cracks [34, 53, 56] or ii) considering implicitly the species diffusion in the cracks. The first strategy leads to local fine mesh and huge computational time [53]. The second strategy involves the modeling of the physics in the cracks. The transport *along* and *across the* discontinuities [34, 56] is taken into account in the discretized domain using boundary conditions [50] or specific assumptions[19, 26, 57].

To avoid local fine mesh inside the discontinuity, we propose here to model the transport both along and across the discontinuities following the dedicated assumptions of [19, 26, 57]. Moreover, the complexity and variety of expertise of IRSN lead to study concrete aging and the storage of nuclear waste in geological formations. These kind of problems need complex chemical modeling to take into account multiple reactions: sorption, solid precipitation, solid dissolution and aqueous reactions [28]. Following the works of [10, 15], in this paper, we derive a generic chemical model able to catch simultaneously all these reactions.

The reactive transport in a discontinuous porous medium remains a challenge due to the strong coupling between the local geochemical reactions and the diffusive problem requiring to capture the fracture network [53]. To illustrate the coupling, the applications focus on the impact of the crack path to one chemical degradation [19, 26, 34, 38, 56] or the reduction of the complexity of the species' diffusion inside the discontinuities through a mean diffusion model

[11, 53]. The novelty of the proposed approach rests on considering a large panel of geochemical reactions within a multibody framework to capture the heterogeneities and the discontinuities.

The paper is organized as follows. Section 2 describes the species transport in a discontinuous heterogeneous medium. Section 3 focuses on the chemical formulation of a porous medium (geochemistry) and in the Section 4, we present the reactive transport model. The reactive transport model is implemented in the IRSN numerical platform XPER [47, 48] and validated by comparison with the HYTEC software [64]. The last section is devoted to numerical experiments. We simulate two well-known chemical reactions in geomaterials: calcium leaching and internal sulfate reactions. The studies highlight the impact of the discontinuities in the reactive transport kinetics as well as the localization effect.

2 Species diffusion in discontinuous-porous medium

Let us consider a porous medium Ω (boundary $\partial\Omega$), divided into N^e subdomains Ω_e such that $\Omega = \bigcup\limits_{e=1,N^e} \Omega_e$ and containing a discontinuity made of two lips $\Gamma_d = \Gamma_d^+ \cup \Gamma_d^-$, see Fig. 1. We consider Dirichlet conditions on a part of the boundary Γ^C and Neumann conditions on its complement $\Gamma^\Phi = \partial\Omega \backslash \Gamma^C$.

The continuum and the discontinuity are assumed to be fully saturated with water. The transport of the N^{aq} aqueous species is split into a volume contribution perturbed by the discontinuity (flow across the discontinuity) and a surface contribution (flow along the discontinuity).
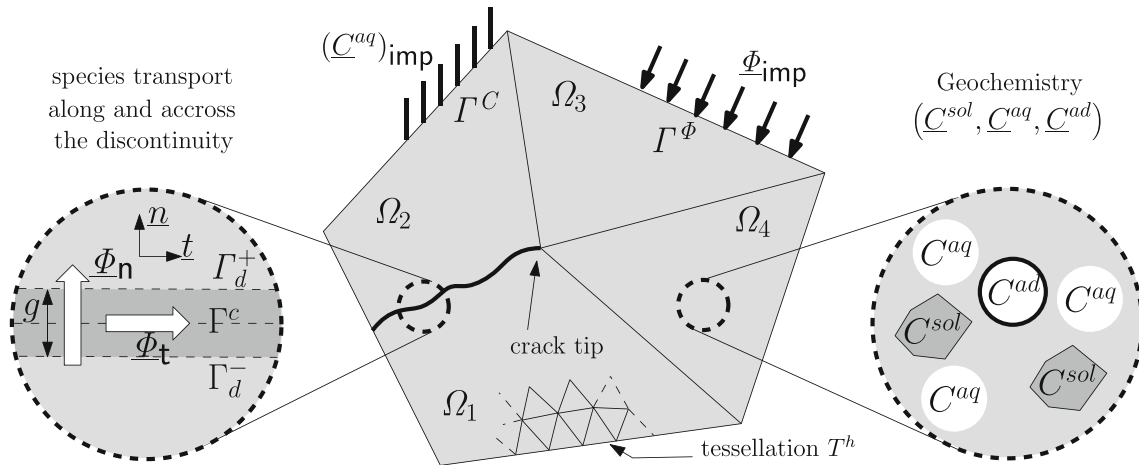

Fig. 1 Sketch of the domain Ω, its partition into Ω_e subdomains ($1 \leq e \leq N^e$), its tessellation T^h and the discontinuity Γ^d

2.1 Transport across the discontinuity

For each aqueous species $i \in [1, N^{aq}]$, the scalar values C_i^{aq} [$mol.L^{-1}$], D_i [$m^2.s^{-1}$], r_i [$mol.L^{-1}.s^{-1}$] denote respectively the concentration, the effective diffusion coefficient and the source term of the species, while the vector $\underline{\Phi}_i$ denotes its flux. These quantities are summed up in a vectorial representation $\underline{C}^{aq} = \langle C_1^{aq}, \cdots, C_{N^{aq}}^{aq} \rangle$, $\underline{r} = \langle r_1, \cdots, r_{N^{aq}} \rangle$, $\underline{D} = \langle D_1, \cdots, D_{N^{aq}} \rangle$, the fluxes are catenated to a matrix $\underline{\underline{\Phi}} = \langle \underline{\Phi}_1, \cdots, \underline{\Phi}_{N^{aq}} \rangle$ and a normal-tangent decomposition is used $\Phi_{ni} = \underline{\Phi}_i \cdot \underline{n}$ and $\underline{\Phi}_{ti} = \underline{\Phi}_i - \Phi_{ni}\underline{n}$, $\forall i \in [1, N^{aq}]$, where $\underline{n}$ is the outward normal vector to Γ_d^+. We assume the transport of ions is mainly driven by the concentration gradient of the species itself and it is modeled by the Fick's law:

$$\forall i \in [1, N^{aq}], \quad \begin{cases} \dfrac{\partial(\phi C_i^{aq})}{\partial t} = -\nabla \cdot (\underline{\Phi}_i) + r_i & \text{in } \Omega \\ \underline{\Phi}_i = -D_i \nabla C_i^{aq} & \text{in } \Omega \\ \underline{\Phi}_i \cdot \underline{n} = (\Phi_i)_{\text{imp}} & \text{on } \Gamma^\Phi \\ C_i^{aq} = (C_i^{aq})_{\text{imp}} & \text{on } \Gamma^C \end{cases} \tag{1}$$

where ϕ is the porosity $[-]$,
$\underline{\Phi}_{\text{imp}} = \langle (\Phi_1)_{\text{imp}}, \cdots, (\Phi_{N^{aq}})_{\text{imp}} \rangle$ are the imposed flux conditions on Γ^Φ and
$(\underline{C}^{aq})_{\text{imp}} = \langle (C_1)_{\text{imp}}, \cdots, (C_{N^{aq}})_{\text{imp}} \rangle$ are the imposed concentration conditions on Γ^C.

The flow across the discontinuity, denoted Φ_{ni}, may induce some resistance to the species transport [4, 26, 57, 65]. The contribution of the discontinuity is defined by the flux Φ_i^+, resp. Φ_i^-, across to Γ_d^+, resp. Γ_d^-:

$$\forall i \in [1, N^{aq}], \quad \begin{cases} \Phi_i^+ \underline{n} = (\Phi_{ni} - q_i^+)\underline{n} & \text{on } \Gamma_d^+ \\ \Phi_i^- \underline{n} = (-\Phi_{ni} - q_i^-)\underline{n} & \text{on } \Gamma_d^- \end{cases} \tag{2}$$

where q_i^+ and q_i^- are the flux parts of the boundaries inside the discontinuity.

Let us consider the space tessellation T^h of Ω, a finite element discretization. A variational statement of the problem is derived and the broken Sobolev spaces X and W are introduced:

$$\begin{aligned} X &= \left\{ w \in [L^2(\Omega)] \mid w_{|\Omega_e} \in [H^1(\Omega_e)], \ \forall \Omega_e \in T^h, \right. \\ & \quad \left. w = (C_i^{aq})_{\text{imp}} \text{ on } \Gamma^C \right\} \\ W &= \left\{ w \in [L^2(\Omega)] \mid w_{|\Omega_e} \in [H^1(\Omega_e)], \ \forall \Omega_e \in T^h, \right. \\ & \quad \left. w = 0 \text{ on } \Gamma^C \right\} \end{aligned} \tag{3}$$

Multiplying the species transport (1) by the virtual concentration field w, integrating over the domain Ω and applying the Green-Ostrogradski's theorem, the following weak problem is obtained:

find $C_i^{aq} \in X$, $\forall i \in [1, N^{aq}]$, such that:

$$\sum_{e=1}^{N^e} \left(\int_{\Omega_e} \frac{\partial(\phi C_i^{aq})}{\partial t} w d\Omega + \int_{\Omega_e} D_i \nabla C_i^{aq} \cdot \nabla w d\Omega \right) =$$
$$\sum_{e=1}^{N^e} \left(\int_{\Omega_e} r_i w d\Omega + \int_{\Gamma_e^\Phi} (\Phi_i)_{\text{imp}} w d\Gamma + \int_{(\Gamma_d^-)_e} \Phi_i^+ w d\Gamma \right.$$
$$\left. + \int_{(\Gamma_d^+)_e} \Phi_i^- w d\Gamma \right), \qquad \forall w \in W$$
$$\tag{4}$$

where the Γ_e^Φ, $(\Gamma_d^+)_e$ and $(\Gamma_d^-)_e$ are a partition of Γ^Φ, Γ_d^+ and Γ_d^- respectively.

To define the concentration gradient across the discontinuity $\Phi_{ni} = -D_i^c \nabla C_i^{aq} \cdot \underline{n}$, a characteristic length e [m] is introduced together with the concentration jump $\left[C_i^{aq} \right]$ [33, 62] and the flux reads [4]

$$\forall i \in [1, N^{aq}], \ \Phi_{ni} = -D_i^c \frac{\left[C_i^{aq} \right]}{e} = -D_i^c \frac{(C_i^{aq})^+ - (C_i^{aq})^-}{e} \tag{5}$$

where $(C_i^{aq})^+$ and $(C_i^{aq})^-$ are respectively the concentrations on Γ_d^+ and Γ_d^-. Note that the characteristic length is generally taken into account in the diffusion term to model resistance flow in the transversal direction of the crack [19, 26, 57, 65].

2.2 Transport along the discontinuity

Let us consider a mid-plane domain of the discontinuity Γ^c, see Figs. 1 and 2, with Dirichlet condition on the boundary $\partial \Gamma^c$. Following [19, 26, 57], the species transport along the discontinuity is assumed to be modeled again by Fick's law written on Γ^c such that:

$$\forall i \in [1, N^{aq}] \text{ on } \Gamma^c,$$
$$\frac{\partial (C_i^{aq})^c}{\partial t} = \nabla \cdot \left(D_i^c \nabla^c (C_i^{aq})^c \right) + r_i^c + q_i^+ + q_i^- \tag{6}$$

where the exponent c denotes any value on the mid-plane, the source terms q_i^+ and q_i^- are the boundary contributions of the flow inside the discontinuity and the gradient ∇^c on the mid-plane is defined as the tangential part of the volume gradient:

$$\forall i \in [1, N^{aq}],$$
$$\underline{\Phi}_{ti} = \nabla^c (C_i^{aq})^c = \nabla (C_i^{aq})^c - \left(\nabla (C_i^{aq})^c \cdot \underline{n} \right) \underline{n} \tag{7}$$

The Sobolev spaces X and W have their counterparts on Γ^c:

$$\begin{aligned} X^c &= \left\{ w^c \in [H^1(\Gamma^c)] \mid w^c = C_{\text{impc}}^{aq} \text{ on } \partial \Gamma^c \right\} \\ W^c &= \left\{ w^c \in [H^1(\Gamma^c)] \mid w^c = 0 \text{ on } \partial \Gamma^c \right\} \end{aligned} \tag{8}$$
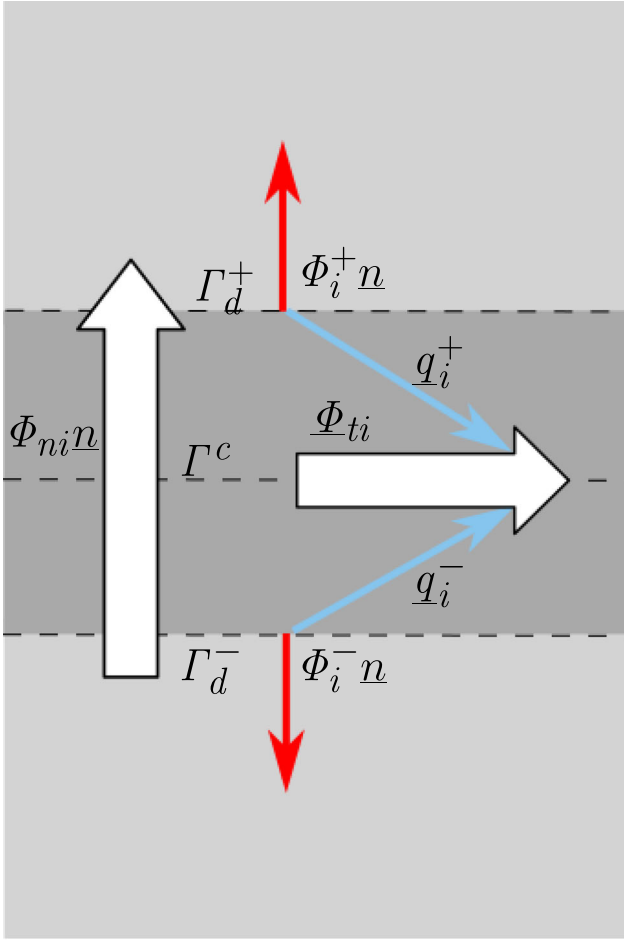
Fig. 2 Sketch of the flows through and across the discontinuity. The contribution of the discontinuity, Φ_i^+ and Φ_i^-, depends on the flux across the discontinuity Φ_{ni} (2) and the crack source terms q_i^+ and q_i^- (6)

where C_{impc}^{aq} is the imposed concentration on $\partial \Gamma^c$.

Multiplying the species transport (6) by the local virtual concentration fields w^c, integrating over the domain Γ^c and

applying the Green-Ostrogradski's theorem, the following weak problem is obtained:

find $(C_i^{aq})^c \in X^c, \forall i \in [1, N^{aq}],$ such that:
$$\int_{\Gamma^c} \frac{\partial (C_i^{aq})^c}{\partial t} w^c d\Gamma + \int_{\Gamma^c} D_i^c \nabla^c (C_i^{aq})^c \cdot \nabla^c w^c d\Gamma =$$

$$\int_{\Gamma^c} \left(r_i^c + q_i^+ + q_i^- \right) w^c d\Gamma, \qquad \forall w^c \in W^c \tag{9}$$

2.3 Discontinuous porous medium

Transport across and along the discontinuities are solved using a multibody approach [47]. Each node of the discrete discontinuity is duplicated using the zero-thickness interface elements of the Goodman type [57]. In this framework, the transport is not explicitly solved in the discontinuity (cf. Fig. 3).

Following [57], we close the system assuming that the values on the mid-plane are the average of the values on the boundaries of the discontinuity Γ_d^+ and Γ_d^-:
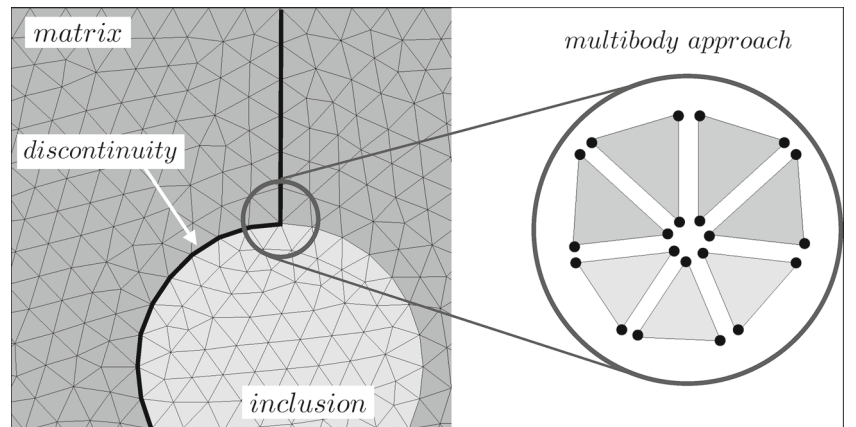
$$\forall i \in [1, N^{aq}],$$
$$(C_i^{aq})^c = \frac{(C_i^{aq})^+ + (C_i^{aq})^-}{2} \overset{\text{def}}{=} \frac{\overline{C_i^{aq}}}{2},$$
$$w^c = \frac{w^+ + w^-}{2}, \quad r_i^c = \frac{r_i^+ + r_i^-}{2} \overset{\text{def}}{=} \frac{\overline{r_i}}{2}, \tag{10}$$

where r^+ and r^- are the source terms in Γ_d^+ and Γ_d^-, and $w^+ \in W$ and $w^- \in W$ are the virtual concentrations in Γ_d^+ and Γ_d^-. Note that, within this framework, there is no unknown on the mid-plane. The assumptions (10) induce the equality of the source term [57]:

$$\forall i \in [1, N^{aq}], \quad q_i^+ = q_i^- \tag{11}$$

Fig. 3 Example of transport spatial discretization. Illustration of the multibody approach

Equation 10 together with Eqs. 2, 4 and 9 lead to the weak formulation of the species transport in the discontinuous medium:

find $(C_i^{aq}) \in X, \forall i \in [1, N^{aq}]$, such that:

$$\sum_{e=1}^{N^e} F_e = 0 \text{ where}$$

$$F_e = \int_{\Omega_e} \frac{\partial(\phi C_i^{aq})}{\partial t} w d\Omega + \int_{\Omega_e} D_i \nabla C_i^{aq} \cdot \nabla w d\Omega +$$

$$+ \int_{(\Gamma_d^+)_e} 0.25 \left(D_i^c \nabla^c \overline{C_i^{aq}} \cdot \nabla^c w + \left(\frac{\partial \overline{C_i^{aq}}}{\partial t} - \overline{r_i} \right) w \right) d\Gamma$$

$$+ \int_{(\Gamma_d^-)_e} 0.25 \left(D_i^c \nabla^c \overline{C_i^{aq}} \cdot \nabla^c w + \left(\frac{\partial \overline{C_i^{aq}}}{\partial t} - \overline{r_i} \right) w \right) d\Gamma$$

$$- \int_{\Omega_e} r_i w d\Omega - \int_{\Gamma_e^\Phi} (\Phi_i)_{\text{imp}} w d\Gamma + \int_{(\Gamma_d^-)_e} D_i^c \frac{[C_i^{aq}]}{e} w d\Gamma$$

$$- \int_{(\Gamma_d^+)_e} D_i^c \frac{[C_i^{aq}]}{e} w d\Gamma, \qquad\qquad \forall w \in W$$
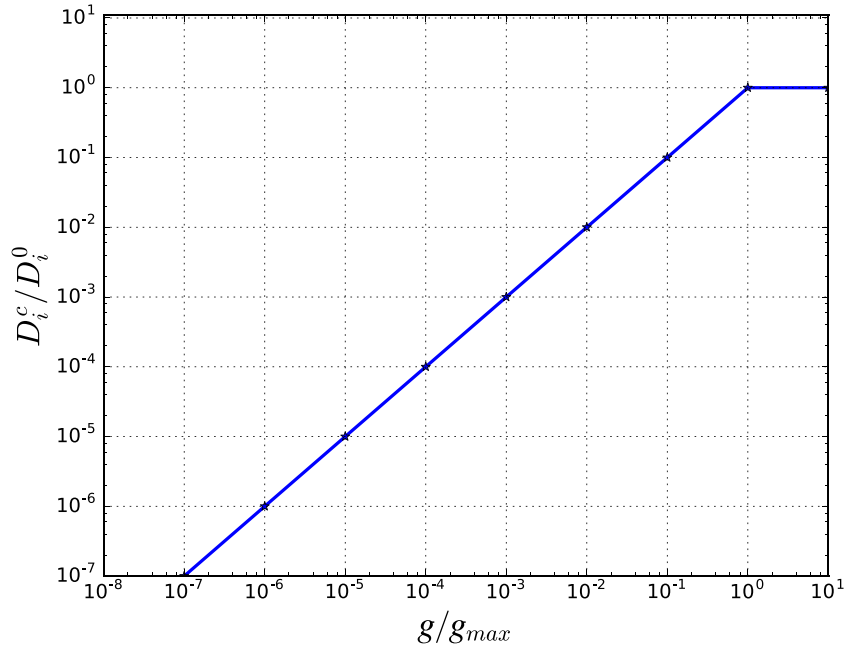
$$(12)$$

2.4 Effective diffusion

2.4.1 Effective diffusion coefficient in the porous medium

The material diffusivity can be estimated through the current microstructure [59, 61] or deduced by the porosity evolution [2, 19, 23]. The second approach is considered using the empirical Archie's law [2]:

$$D_i(\phi) = D_i(\phi_0) \left(\frac{\phi - \phi_c}{\phi_0 - \phi_c} \right)^m \qquad (13)$$

where the ϕ_0 is the initial porosity, $D_i(\phi_0)$ is the initial diffusion coefficient, ϕ_c is a critical porosity threshold under which diffusion stops and m is an empirical Archie's coefficient.

2.4.2 Effective diffusion coefficient along the discontinuity

Based on the experimental work of [13] and on the model of [19], in a saturated medium the effective diffusion coefficient along the discontinuity is assumed to evolve linearly with the gap g between each lips (see Fig. 1) until a critical value g_{max} [m] is reached. Beyond this threshold, the diffusivity remains constant and approximately equal to the diffusivity in liquid phase D_i^0 [$m^2.s^{-1}$] (cf. Fig. 4):

$$\forall i \in [1, N^{aq}], \quad \begin{cases} D_i^c = D_i^0 \dfrac{g}{g_{\text{max}}} & \text{if } g < g_{\text{max}} \\ D_i^c = D_i^0 \end{cases} \qquad (14)$$

Moreover, as in [13, 38, 50, 56], the effective diffusion coefficient is assumed to be isotropic.

3 Geochemistry

3.1 Main assumptions

The geochemistry model is mainly based on the work of [10, 14, 15]. The porous medium Ω is composed of N^{aq} aqueous, N^{ad} sorbed and N^{sol} solid chemical species (see Fig. 1). The evolution of the aqueous species by diffusion process induces chemical reactions and microstructure changes. Let us consider the system composed of N^r

Fig. 4 Effective diffusion coefficient along the discontinuity vs gap between each boundaries

reactions between N^l (where $N^l = N^{aq} + N^{ad} + N^{sol}$) chemical species described by:

$$\forall j \in [1, N^r], \quad \sum_{i=1}^{N^l} S_{i,j}^p \left(X_i^p\right)^{z_i} \leftrightharpoons 0 \qquad (15)$$

where the exponent p denotes the phase, $\underline{\underline{S}}^p \in (\mathbb{R})^{N^l \times N^r}$ is the stoichiometric coefficients matrix $[-]$, $\underline{X}^p \in (\mathbb{R}^+)^{N^l}$ is the chemical component (reactant and product) and $\underline{z} \in \mathbb{R}^{N^l}$ is the valence of species vector $[-]$. The phase p can be aqueous, sorbed or solid, respectively denoted aq, ad and sol. We assume the following assumptions.

1. *The solution is diluted.*
    The aqueous activity $\underline{a}^{aq} \in (\mathbb{R}^+)^{N^{aq}}$ depends on the activity coefficient $\underline{\gamma} \in (\mathbb{R}^+)^{N^{aq}}$ $[-]$, on the species concentration $\underline{C}^{aq} \in (\mathbb{R}^+)^{N^{aq}}$ and on the reference concentration C_{ref} $[mol.L^{-1}]$ (by default equals to $1\ mol.L^{-1}$) [31, 63]:

    $$\forall i \in [1, N^{aq}], \quad a_i^{aq} = \frac{\gamma_i C_i}{C_{ref}} \qquad (16)$$

    For small ionic strength I_s ($< 0.3\ mol.kg^{-1}$), the term of chemical activity can be evaluated by the so-called truncated Davies' law [30, 37, 55]:

    $$\forall i \in [1, N^{aq}], \begin{cases} I_s = \frac{1}{2} \sum_{i=1}^{N^{aq}} z_i^2 C_i^{aq} \\ \ln(\gamma_i) = -A z_i^2 \left(\frac{\sqrt{I_s}}{1+\sqrt{I_s}} - b I_s \right) \end{cases} \qquad (17)$$

    where A and b are parameters.
2. *The local equilibrium assumption:*
    The chemical processes are in thermodynamical equilibrium. In geomaterials, it is common to consider that the kinetic of reactive transport is driven by the diffusion of species [10, 15, 55]. This assumption induces that the chemical reactions are reversible and are fast enough compared to the species transport. The validity of the local equilibrium assumption is justified if the dimensionless Damköhler number D_a [30, 55] is greater than 1 ; with:

    $$D_a = \frac{t_d}{t_r} \qquad (18)$$

    where t_r and t_d denote respectively the chemical reaction time and the diffusion time $[s]$. Following [55], we assume also a reactive time of $100\ s$. The characteristic diffusion time is described by:

    $$t_d = \frac{l_c^2}{D} \qquad (19)$$

where l_c is a characteristic diffusion length which corresponds to the main element size. In Section 6, the element size is chosen equal to $2\ mm$.

Considering in our applications a maximum diffusivity of $10^{-9}\ m^2.s^{-1}$, the Damköhler number D_a is thus equal to 40 ($>> 1$).

3. The solid activity is equal to one.
4. The activity of the adsorbed species is equal to the concentration [10, 14].

3.2 Law of mass action

Each chemical reaction has to obey the law of mass action in order to ensure the thermodynamical equilibrium of the system:

$$\forall j \in [1, N^r], \quad \left(K_j^p\right)^{-1} \prod_{i=1}^{N^l} \left(a_i^p\right)^{S_{i,j}^p} = 1 \qquad (20)$$

where $\underline{K}^p \in (\mathbb{R}^+)^{N^r}$ is the vector of equilibrium constants of the reaction $[-]$ and $\underline{a}^p \in (\mathbb{R}^+)^{N^l}$ is the vector of species activities $[-]$ of the phase p. The species activity depends on the considered phase.

3.3 Aqueous reactions

The aqueous reactions involve an aqueous solution where the reactant and the product are in the aqueous phase. These reactions take into account hydrolysis, oxidation-reduction and acid base reactions. In reactive transport, it is common to distinguish primary and secondary components [10, 31, 35, 63, 64]. The secondary components $\underline{C}^{aq,s} \in (\mathbb{R}^+)^{N^{aq,s}}$ are obtained by a linear combination of the primary components $\underline{C}^{aq,p} \in (\mathbb{R}^+)^{N^{aq,p}}$ using the law of mass action (20):

$$\forall i \in [1, N^{aq,s}], \quad C_i^{aq,s} = \frac{K_i^{aq}}{\gamma_i} \prod_{j=1}^{N^{aq,p}} \left(\frac{\gamma_j C_j^{aq,p}}{C_{ref}} \right)^{S_{i,j}^{aq}} \qquad (21)$$

where $N^{aq} = N^{aq,p} + N^{aq,s}$, $\underline{K}^{aq} \in (\mathbb{R}^+)^{N^{aq,s}}$ is the vector of aqueous equilibrium constants and $\underline{\underline{S}}^{aq} \in (\mathbb{R}^+)^{N^{aq,s} \times N^{aq,p}}$ is the stoichiometric coefficients matrix of aqueous reactions.

3.4 Sorption reactions

In a fluid-solid structure, the sorption consists in the accumulation of fluid at the interface of the solid [1]. In geomaterial, the sorption phenomena can be modeled with solid solution models [27] or with surface complexation and ions exchanges [10, 16]. The surface complexation is modeled here. Based on the law of mass action, the $N^{ad,s}$

secondary concentrations $\underline{C}^{ad,s} \in (\mathbb{R}^+)^{N^{ad,s}}$ are obtained from the $N^{ad,p}$ primary concentrations $\underline{C}^{ad,p} \in (\mathbb{R}^+)^{N^{ad,p}}$:

$$\forall i \in [1, N^{ad,s}],$$
$$C_i^{ad,s} = K_i^{ad} \prod_{j=1}^{N^{aq,p}} \left(\frac{\gamma_j C_j^{aq,p}}{C_{ref}} \right)^{S_{i,j}^{ad/aq}} \prod_{u=1}^{N^{ad,p}} \left(C_u^{ad,p} \right)^{S_{i,u}^{ad/ad}}$$
(22)

where $N^{ad} = N^{ad,p} + N^{ad,s}$, $\underline{K}^{ad} \in (\mathbb{R}^+)^{N^{ad,s}}$ is the vector of sorption equilibrium constant, $\underline{\underline{S}}^{ad/ad} \in (\mathbb{R}^+)^{N^{ad,s} \times N^{ad,p}}$ and $\underline{\underline{S}}^{ad/aq} \in (\mathbb{R}^+)^{N^{ad,s} \times N^{aq,p}}$ are the stoichiometric coefficients matrix of the sorption reaction. The present model does not change the sorption equilibrium constant by the surface potential rather than in [16].

The sorbed model is closed by the mass conservation of fixed concentration (relation of occupied sites) [1, 10]:

$$\underline{C}_{tot}^{ad} - \left[\underline{C}^{ad,p} + \left(\underline{\underline{S}}^{ad/ad} \right)^T \cdot \underline{C}^{ad,s} \right] = \underline{0}$$
(23)

where $\underline{C}_{tot}^{ad} \in (\mathbb{R}^+)^{N^{ad,p}}$ is the total concentration vector of sorbed sites.

3.5 Solid reactions

Solid reactions are heterogeneous reactions between aqueous and solid phases. Since the solid activity is equal to one and the precipitation-dissolution reactions are assumed to be static, the solid concentration could not be directly deduced from primary aqueous concentration. The law of mass action must be satisfied to ensure the thermodynamic balance of each solid:

$$\forall i \in [1, N^{sol}],$$
$$\xi_i^{sol} \left(\underline{C}^{aq,p} \right) \overset{\text{def}}{=} \left(K_i^{sol} \right)^{-1} \prod_{j=1}^{N^{aq,p}} \left(a_j^{aq,p} \right)^{S_{i,j}^{sol}} - 1 = 0 \quad (24)$$

where N^{sol} is the number of precipitation-dissolution reactions, $\underline{K}^{sol} \in (\mathbb{R}^+)^{N^{sol}}$ is the dissolution equilibrium constant vector and $\underline{\underline{S}}^{sol} \in (\mathbb{R}^+)^{N^{sol} \times N^{aq,p}}$ is the stoichiometric matrix of the solid reactions. To ensure the positivity of the concentrations, the solid reactions problem could be written as a complementary problem [15]. In this work, we consider the solid concentration strictly positive and we use a dedicated solving in case of a total dissolution

[59]. The solid reactions model is closed by the mass conservation relations of the aqueous species:

$$\underline{C}_{tot}^{aq} - \left[\underline{C}^{aq,p} + \left(\underline{\underline{S}}^{sol} \right)^T \cdot \underline{C}^{sol} \right] = \underline{0} \quad (25)$$

where $\underline{C}_{tot}^{aq,p} \in (\mathbb{R}^+)^{N^{ad,p}}$ is the total aqueous concentration vector.

3.6 Electroneutrality constraint

In this work, to take into account the electronic impact of the solution in the thermodynamic equilibrium of the system we add the the activity coefficient to the work of [10, 15]. Furthermore, we can impose the electroneutrality:

$$\underline{z} \cdot \underline{C}^{aq} = 0 \quad (26)$$

3.7 Geochemistry reactions

The geochemical model writes:

find $\underline{C}^{aq,p} \in (\mathbb{R}_+)^{N^{aq}}$,
$\underline{C}^{ad,p} \in (\mathbb{R}_+)^{N^{ad}}, \underline{C}^{sol} \in (\mathbb{R}_+^*)^{N^{sol}}$ such that:
$$\begin{cases} \underline{C}_{tot}^{aq} - \left[\underline{C}^{aq,p} + (\underline{\underline{S}}^{aq})^T \cdot \underline{C}^{aq,s} + (\underline{\underline{S}}^{ad/aq})^T \cdot \underline{C}^{ad,s} \right. \\ \left. + (\underline{\underline{S}}^{sol})^T \cdot \underline{C}^{sol} \right] = \underline{0} \\ \underline{C}_{tot}^{ad} - \left[\underline{C}^{ad,p} + \left(\underline{\underline{S}}^{ad/ad} \right)^T \cdot \underline{C}^{ad,s} \right] = \underline{0} \\ \underline{\xi}^{sol} \left(\underline{C}^{aq} \right) = \underline{0}, \qquad \underline{z} \cdot \underline{C}^{aq} = 0 \end{cases}$$
(27)

To ensure the positivity of all concentrations, the law of mass action is rewritten with logarithmic unknown [10, 60]:

$$\begin{cases} \forall i \in [1, N_s^{aq}], \\ C_i^{aq,s} = \\ \exp \left[\ln(K_i^{aq}) - \ln(\gamma_i) + \sum_{j=1}^{N^{aq,p}} S_{i,j}^{aq} \left(\ln(\gamma_j) + \ln \left(C_j^{aq,p} \right) \right) \right] \\ \forall i \in [1, N_s^{ad}], \\ C_i^{ad,s} = \\ \exp \left[\ln(K_i^{ad}) + \sum_{j=1}^{N^{aq,p}} S_{i,j}^{ad/aq} \left(\ln(\gamma_j) + \ln \left(C_j^{aq,p} \right) \right) \right. \\ \left. + \sum_{j=1}^{N^{ad,p}} S_{i,j}^{ad/ad} \ln \left(C_j^{ad,p} \right) \right] \\ \forall i \in [1, N^{sol}], \\ \xi_i^{sol*} \left(\underline{C}^{aq} \right) \overset{\text{def}}{=} \\ - \ln(K_i^s) + \sum_{j=1}^{N^{aq,p}} S_{i,j}^{sol} \left(\ln(\gamma_j) + \ln \left(C_j^{aq,p} \right) \right) \end{cases}$$
(28)

The mass action law is specified in the Appendix 1. The system is thus rewritten:

find $\underline{C}^{aq,p} \in (\mathbb{R}_+^*)^{N^{aq}}$, $\underline{C}^{ad,p} \in (\mathbb{R}_+^*)^{N^{ad}}$ and $\underline{C}^{sol} \in (\mathbb{R}_+^*)^{N^{sol}}$ such that:

$$
\begin{cases}
\underline{C}_{tot}^{aq} - \left[\exp\left(\ln\left(\underline{C}^{aq,p} \right) \right) + \left(\underline{\underline{S}}^{aq} \right)^T \cdot \underline{C}^{aq,s} \right. \\
\qquad \left. + \left(\underline{\underline{S}}^{ad/aq} \right)^T \cdot \underline{C}^{ad,s} + \left(\underline{\underline{S}}^{sol} \right)^T \cdot \underline{C}^{sol} \right] = \underline{0} \\
\underline{C}_{tot}^{ad} - \left[\exp\left(\ln\left(\underline{C}^{ad,p} \right) \right) + \left(\underline{\underline{S}}^{ad/ad} \right)^T \cdot \underline{C}^{ad,s} \right] = \underline{0} \\
\underline{\xi}^{sol*} \left(\underline{C}^{aq,p} \right) = \underline{0}, \qquad \sum_{i=1}^{N_p^{aq}+N_s^{aq}} z_i \exp\left(\ln\left(C_i^{aq} \right) \right) = 0
\end{cases}
$$

(29)

The uniqueness of the solution is demonstrated by [15]. The system is solved using the Newton-Raphson method (see Appendix 2). In the case of a total solid dissolution, the strict positivity of the concentration is assured by an elimination method. Additional information on the numerical methods is described in [59].

3.8 Porosity evolution

Such as the diffusion coefficient, we assume that the porosity evolution depends only of the solid concentrations [24]:

$$
d\phi = \frac{-\sum_{i}^{N^{sol}} \phi v_i dC_i^{sol}}{1 + \sum_{i}^{N^{sol}} v_i C_i^{sol}}
$$

(30)

where $\underline{v} \in \left(\mathbb{R}^+ \right)^{N^{sol}}$ is the molar volume vector $[L.mol^{-1}]$.

4 Reactive transport

The reactive transport in the discontinuous and heterogeneous medium rests both on the coupling between species transport in discontinuous medium (Section 2) and geochemistry (Section 3) and on a multibody approach. The physical models are implemented in the IRSN XPER framework [47, 48], dedicated to Discrete and Finite Element method with massively parallel computation capability in the context of non smooth behavior law. It is devoted to the study of dynamic fracture of heterogeneous materials with strong multi-physics coupling [4, 12].

Modeling reactive transport problems leads to a highly non linear coupled system requiring the use of a coupling framework. In this study, for the sake of simplicity and to improve each model independently, a so-called Sequential

Non-Iterative Approach (SNIA) is implemented [10], see Fig. 5. From a numerical point of view, a specific software can be easily coupled for solving each model, i.e. chemical model with CHESS [63] or PHREEQC [43]. However, such an approach requires small time steps [1, 10].

The time discretization of the diffusion species can be set from fully explicit to implicit, with a centered (Crank–Nicholson) approach using the θ-method integration. In the following, the time discretization is fully implicit with $\theta = 1$. The geochemistry is considered to be static. The transport solver gives all concentrations at each node of the volumetric finite elements and the chemistry is also solved at these nodes. This strategy is used by different authors [25, 36, 43] and ensures both the stability of the system and the positivity of the concentrations at the end of the time step. The multibody approach allows modeling heterogeneous media where each element is dedicated to a specific material, Fig. 3. In particular, we do not need to model the transition zone between each materials with a specific element.

As described in [25], the Dirichlet conditions of the species transport problem affect the chemical model and induce an accurate solving for the geochemistry problem. An elimination strategy is implemented and when all concentrations are imposed, the geochemical problem is not solved at these nodes.

In the MoMas benchmark, [23] and [32] shown that a coarse mesh can generate numerical oscillations in the solution profile as does the temperature in a thermal shock: a rapid change in local species concentration can lead to a high local concentration gradient and can induce instability. To ensure the stability, the criterion proposed by [44] is generalized for the diffusion of species in heterogeneous media:

$$
\Delta t > \max_p \left(\frac{\phi^p}{4D^p} l_c^2 \right)
$$

(31)

where Δt is the time step $[s]$, l_c is the characteristic mesh size $[m]$ and ϕ^p and D^p are respectively the porosity and the species coefficient of the phase p. For practical purpose, the criterion (31) is a rough estimate and the final convenient
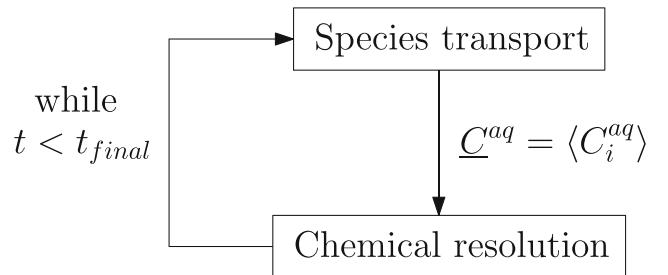

Fig. 5 Diagram of the Sequential Non-Iterative Approach coupling strategy

Table 1 Validation: diffusion parameters

$D \; [m^2.s^{-1}]$	10^{-11}
ϕ	0.1

Table 2 Aqueous reaction validation: chemical parameters

	B1	B2	Initial conditions
$C^{aq}_{Ca^{2+}} \; [mol.L^{-1}]$	0.	0.05	0.02
$C^{aq}_{NO_3^-} \; [mol.L^{-1}]$	0.5	0.	0.1
$C^{aq}_{CaNO_3^+} \; [mol.L^{-1}]$	0.	0.	6.387×10^{-3}

time step is adjusted depending on the largest concentration gradient over all the species.

5 Validation

The validation of the numerical framework and its software implementation rests on the comparison with results obtained using the HYTEC reference software [64]. HYTEC is a finite volume software that integrates a wide variety of features and options based on the coupling of two codes CHESS [63] and R2D2 [64]. This software has successfully participated in different benchmarks [9, 49].

We consider a homogeneous porous medium, with a constant porosity. The local diffusion properties are summarized in Table 1. The thermodynamic database THERMODEM 17 [6] is used and the truncated Davie's law parameters (17) are $A = 1.13$ and $b = 0.25$ [37, 59]. Let us consider a long and thin rectangular domain Ω ($10 \times 0.5 mm^2$) between two batches B_1 and B_2. The chemical of each batch is taken into account by imposing the concentrations on the domain boundaries. Homogeneous Neumann conditions are imposed on the other boundaries, Fig. 6. Three chemical reactions are studied: aqueous reaction, solid reaction and solid reaction with imposed electroneutrality. For each case, the agreement between both solutions is quantified with an L_2 norm of the relative error.

5.1 Aqueous reaction: calcium nitrate complexation

The calcium nitrate complexation reads ($\log_{10}(K^{aq}) = 0.7$):

$$\left(Ca^{2+} \right)^{aq} + \left(NO_3^- \right)^{aq} \leftrightharpoons \left(CaNO_3^+ \right)^{aq}, \tag{32}$$

The boundary conditions, the initial conditions and the constitutive model parameters are summarized in Table 2. The time step is $\Delta t = 1000s$ and the characteristic mesh size is $l_c = 2 \times 10^{-5}m$.

Two cases are considered: without and with chemical activity Eq. (16–17 with $A = 1.13$ and $b = 0.25$). The
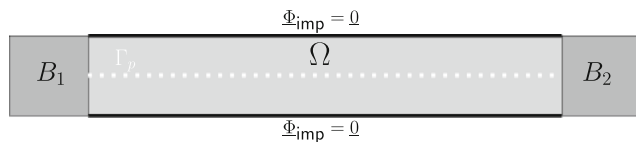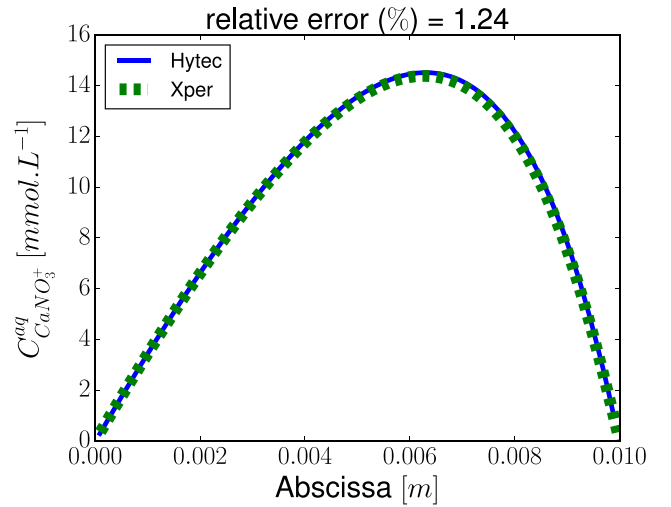
Fig. 7 shows the calcium nitrate complex concentrations at 10 days obtained with XPER and HYTEC for the two cases. The relative errors are lower than 1.3%, which validates the aqueous reaction case.

(a)

(b)

Fig. 7 Aqueous reaction validation: $CaNO_3^+$ concentration along the axis Γ_p at 10 days **a** without activity coefficient, **b** with activity coefficients $A = 1.13$ and $b = 0.25$

Fig. 6 Aqueous reaction validation: sketch of the study case. Domain Ω with horizontal axis Γ_p is located between two batches B_1 and B_2
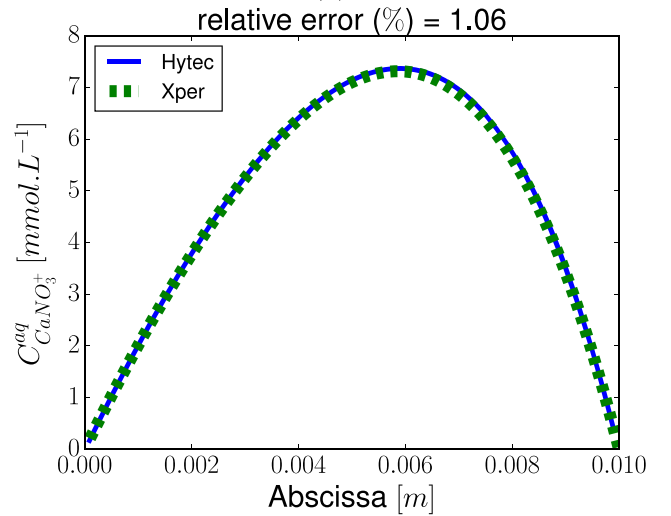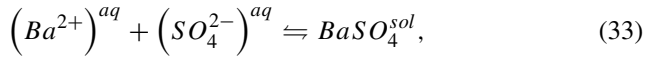
Table 3 Solid reaction validation: chemical parameters

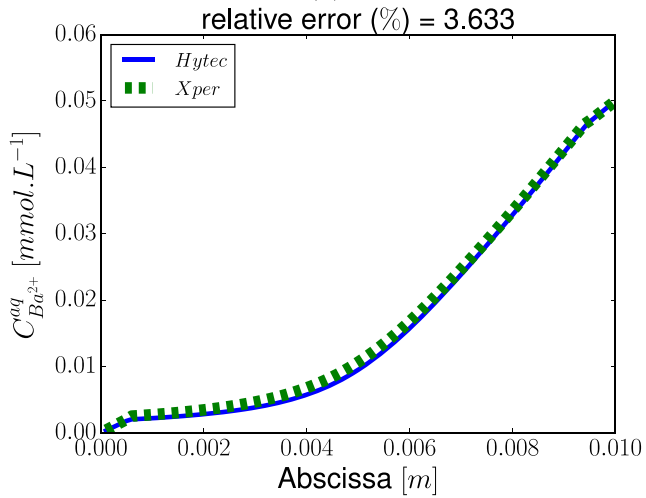|	B1	B2	Initial conditions
$C_{Ba^{2+}}^{aq}[mol.L^{-1}]$	0.	0.05	1.
$C_{SO_4^{2-}}^{aq}[mol.L^{-1}]$	0.05	0.	1.
$C_{BaSO_4}^{sol}[mol.L^{-1}]$	–	–	0.

5.2 Solid reaction: baryte precipitation

The baryte $BaSO_4^{sol}$ precipitation writes ($\log_{10}\left(K^{sol}\right) = -9.9711$):

$$\left(Ba^{2+}\right)^{aq} + \left(SO_4^{2-}\right)^{aq} \leftrightharpoons BaSO_4^{sol}, \qquad (33)$$

Parameters are given in Table 3 and time step is $\Delta t = 50s$. The Fig. 8 shows the baryte and the Ba^{2+} concentrations
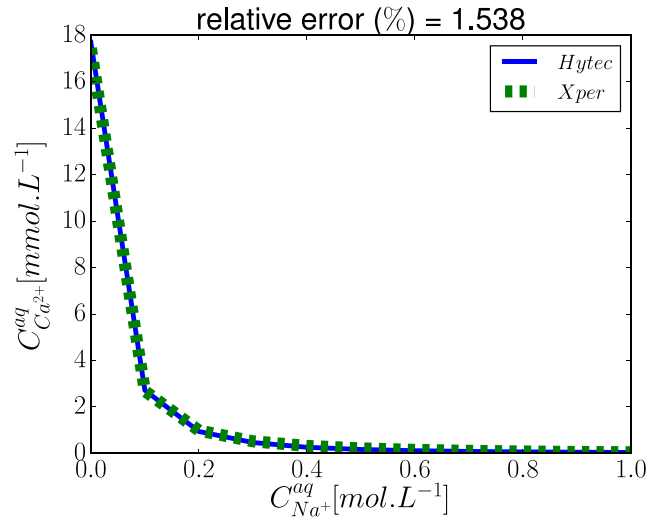

(a)

(b)

Fig. 8 Solid reaction validation, concentrations along the axis Γ_p at 10 days (a) baryte and (b) Ba^{2+}
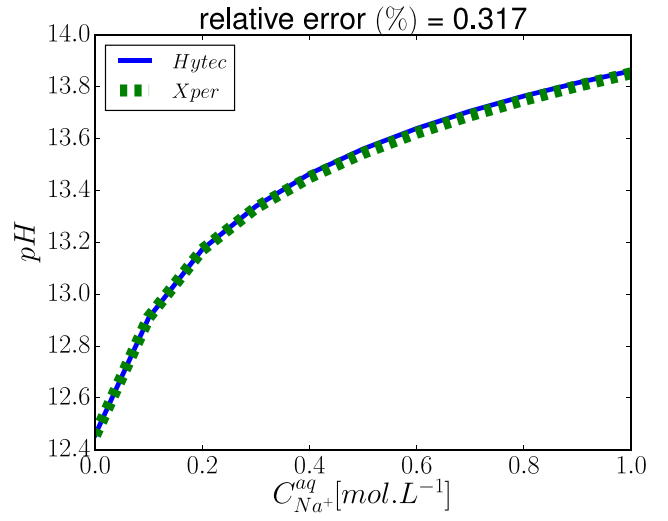
at 10 days obtained with XPER and HYTEC. The relative errors, lower than 7.5%, are due to the transition between dissolution and precipitation of the baryte phase which is quite different between the two codes. The main difference is due to the discretization used by the two codes: Volume Element for HYTEC and Finite Element for XPER. Nevertheless, the relative errors are low enough to validate the solid reaction case.

5.3 Solid reaction with imposed electroneutrality

In a porous medium with only portlandite, the calcium evolution as a function of sodium is studied

(a)

(b)

Fig. 9 Validation of the electroneutrality solving: **a** equilibrium between alkalis and calcium ions and **b** equilibrium between alkalis and pH
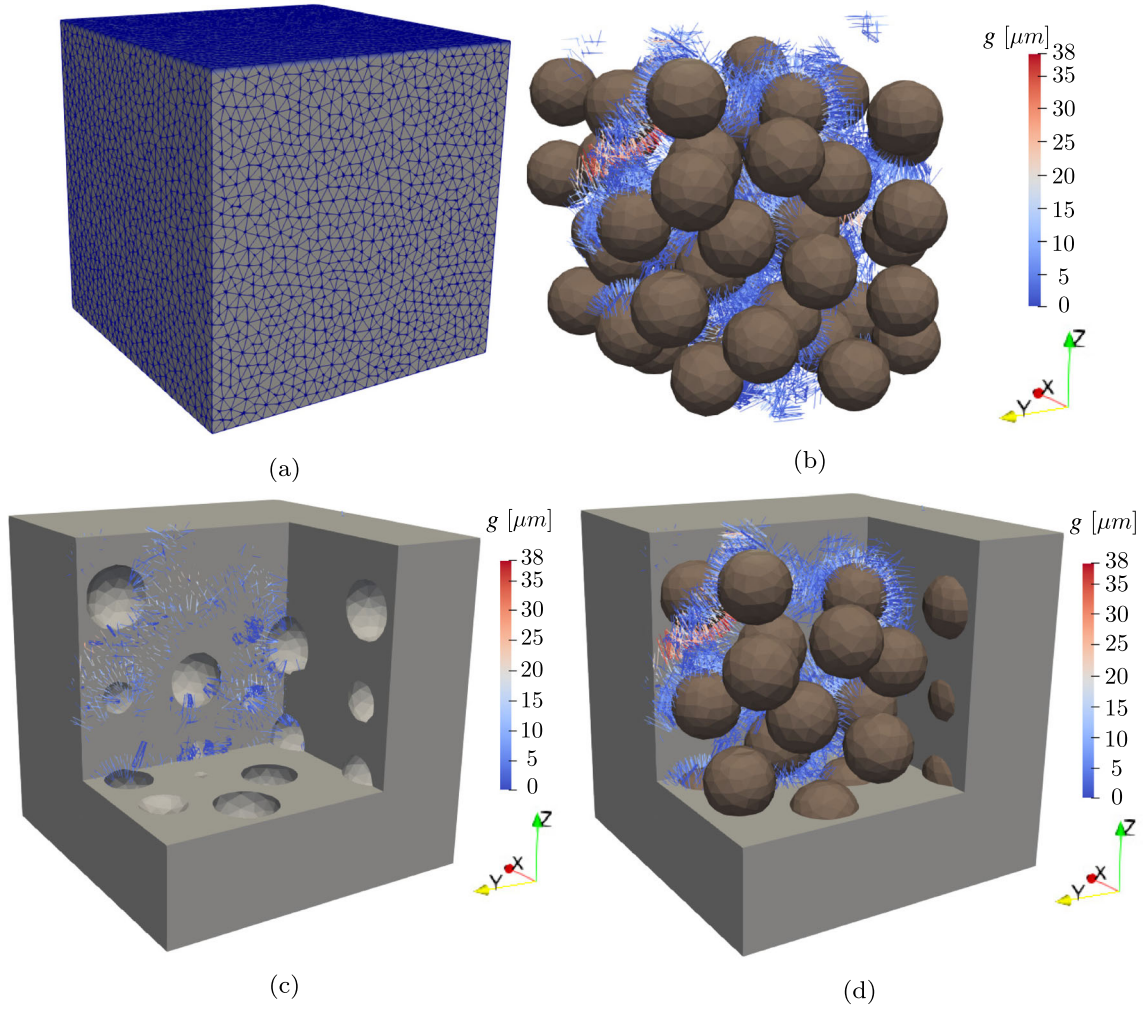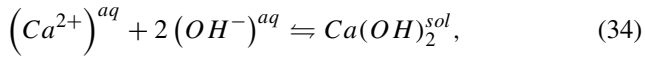
Fig. 10 Pre-cracked concrete sample used for the application: **a** mesh, **b** aggregate and crack path inside the sample, a large gap g corresponds to a crack, **c** cut out in the sample showing the crack path and **d** the influence of the aggregate

$\left(\log_{10} \left(K^{sol} \right) = -5.19 \right)$:

$$\left(Ca^{2+} \right)^{aq} + 2 \left(OH^- \right)^{aq} \leftrightharpoons Ca(OH)_2^{sol}, \tag{34}$$

Since the different aqueous reaction between each ions are taken into account with the electroneutrality equation, this equation helps reducing the number of unknown fields [37, 52, 59]. The Fig. 9 shows the evolution of the equilibrium between alkalis and calcium ions and between alkalis and pH. The relative errors are lower than 1.6%, validating the electroneutrality implementation.

6 Applications

The applications focus on the chemical degradations of a pre-cracked concrete sample by two kinds of chemical attack: Calcium leaching (Section 6.1) and Internal Sulphate Attack (Section 6.2).

We consider a cube ($5 \times 5 \times 5$ cm^3) constituted of a cement paste matrix with 35% volume fraction of aggregates, Fig. 10a. The matrix phase is composed of a CEM I cement paste based on the formulation described by [51]. The temperature is constant $T = 25°C$. The porosity evolves according to the Eq. (30). The initial chemical properties and the initial diffusion parameters where estimated in [59] and are given in Tables 4 and 5. The electroneutrality is imposed to reduce the number of

Table 4 Initial chemical parameters estimated by [59] for the cement paste composition described in [51]

	Concentration [mol/L of water]
C-S-H	14.3
Portlandite	26.05
Ettringite	0.92
Katoite	2.3

Table 5 Diffusion coefficients for the cement paste composition described in [51]

Parameters	Matrix	Aggregates
$D_i(\phi_0)\ [m^2.s^{-1}]$	$7.64\text{x}10^{-12}$	$2.7\text{x}10^{-14}$
$\phi_0[-]$	0.274	0.03
$m[-]$	3.	3.
$\phi_c[-]$	0.	0.
$D_i^0\ [m^2.s^{-1}]$	10^{-9}	10^{-9}
$e[m]$	10^{-8}	10^{-8}

The initial properties was estimated by [59]

chemistry fields. Following [9, 31, 49], we suppose that the diffusion coefficients of the species are equal to each other.

The sample is initially pre-cracked: the discontinuities are localized around the aggregates and through the matrix, Fig. 10 a, b and c. This crack path is typical of delayed strain obtained by sulfate attack [19], drying shrinkage [18] or thermal dilation [4].

The gap of the crack g is not constant and varies within $[0; 38\mu m]$ with a mean value $\bar{g} = 5.3\mu m$. The mean crack density $\bar{\epsilon}$ reads [7]:

$$\bar{\epsilon} = \frac{2N}{\pi} \left\langle \frac{\mathcal{A}^2}{\mathcal{P}} \right\rangle \tag{35}$$

where N is the number of cracks by volume, $\mathcal{A}$ and $\mathcal{P}$ are respectively the area and the perimeter of the discontinuity and the brackets denote the spatial average. Here, the mean crack density $\bar{\epsilon} = 4 \times 10^{-6}$ is relatively low due to the small crack width and the localization of the degradation. If we consider only a sub-volume of $2 \times 5 \times 5\ cm^3$ around the discontinuities, the local crack density ϵ_l is about 10^{-5}.

To study the influence of the gap on the reactive transport, four crack opening critical values g_{max}, see Eq. 14, are considered: without discontinuity $g_{max} = \infty$, small $g_{max} = 100\mu m$, medium $g_{max} = 10\mu m$ and large $g_{max} = 1\mu m$. The Table 6 shows the corresponding value of the mean crack width $\bar{g}$ and the crack density ϵ and the local crack density ϵ_l for each value of g_{max}.

For each chemical attack, the concentrations are imposed on the top boundary domain (in blue in the Fig. 10a) and homogeneous Neumann conditions are imposed on the other boundaries. The domain is discretized with 53942 elements and 2.15×10^5 degrees of freedom for each field.

Table 6 Characteristic of the discontinuities for each crack opening critical value g_{max}

$g_{max}\ [\mu m]$	$\bar{g}\ [\mu m]$	$\bar{\epsilon}$	ϵ_l
100	5.3	4×10^{-6}	10^{-5}
10	53.	4×10^{-4}	10^{-3}
1	530.	3.6×10^{-2}	9.1×10^{-2}

Table 7 Equilibrium table for the leaching and hydration simulation [6, 27]

	C-S-H	Portlandite	Ettringite	Katoite
Ca^{2+}	1.667	2	4	3
OH^-	2.33	1	6	4
$Al(OH)_4^-$	0	0	2	2
SO_4^{2-}	0	0	3	0
$SiO(OH)_3^-$	1	0	0	0
$\log_{10}(K^{sol})$	-13.16	-5.19	-44.9	-20.5

The calcium leaching simulations take into account 9 fields (Section 6.1) and the Internal Sulphate Attack simulations take into account 11 fields (Section 6.2). Each simulation required about 48h on 36 processors (blades composed of 24 "Intel(R) Xeon(R) Gold 6126 CPU @ 2.60GHz" with 192Go of RAM each connected by Infiniband FDR 56Gb/s).
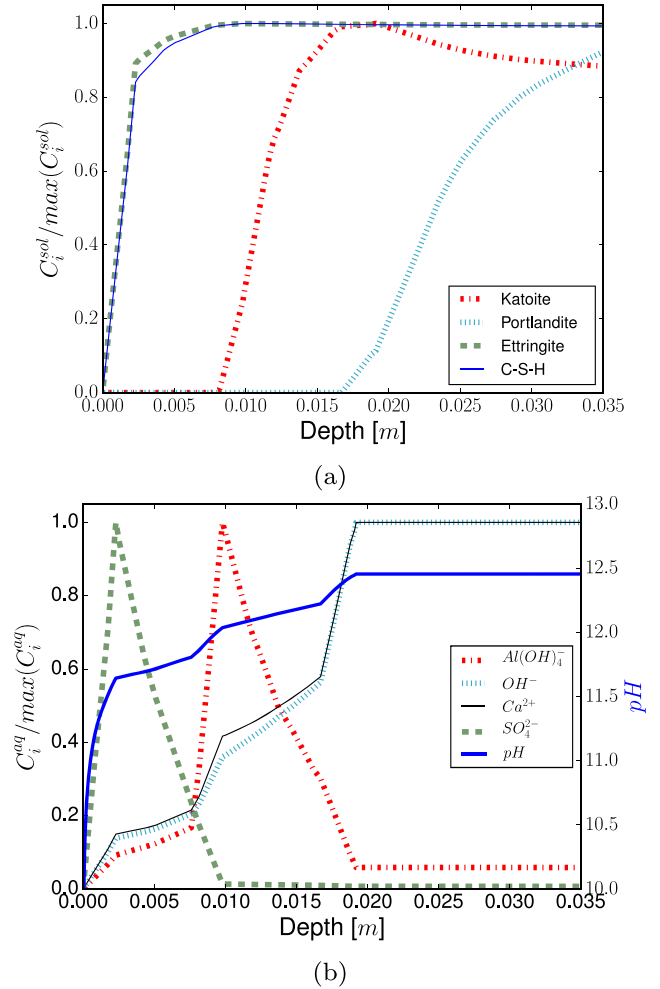

(a)

(b)

Fig. 11 Calcium leaching: concentrations at 13750 days, about 40 years: **a** solid concentrations fraction and **b** aqueous concentrations fraction and pH in solution

6.1 Calcium leaching

The Calcium leaching occurs when concrete structure is in contact with a low pH environment and with few calcium concentrations such as: dams, nuclear waste containment structures, pipes, water storage tanks or tunnels. Calcium leaching induces the migration of the calcium ions from the pore solution to the environment that lead to a progressive dissolution of the cement solid phases called hydrates. The dissolution induces the reduction of the material properties, such as the diffusion coefficients, the elastic properties, the toughness, etc. [17, 20, 61].

In this paper, we study the dissolution of the main phases of the cement paste: ettringite, katoite, portlandite and calcium-silicate-hydrate denoted C-S-H. The chemical reactions, the aqueous component and the equilibrium constant are described in Table 7. We assume that the aggregates are not reactive. We impose a null concentration for all ions except the hydroxide OH^- representing a contact with a solution with a $pH = 7$.

The Fig. 11a shows the solid concentration fractions at 13750 days, about 40 years, in the degraded zone. As

described by various authors [17, 39, 41, 61], we observe three areas from top to bottom:

1. an area with only C-S-H and ettringite,
2. an area with only C-S-H, katoite and ettringite,
3. an area with all the solid phases: C-S-H, katoite, ettringite and portlandite.

The dissolution of the main solid phases induces the evolution of the ions' concentrations and the pH represented in the Fig. 11b. As described in [39], the pH is stabilized around 12.5 by the portlandite phase. The dissolution of the portlandite and of the other solid phases induces the decrease of the pH. The Fig. 12 shows the portlandite field at 4600 days, about the mid of the second decade. The flow inside the discontinuity accelerates the calcium leaching and thus induces dissolution in areas around the crack path. This local dissolution induces some safe zones where the calcium leaching is less pronounced than without cracks. *The flow inside the discontinuities affects the chemical reactions and modifies both the values and the spatial distribution of the species.* Note that the local areas of dissolution around the discontinuity increases with
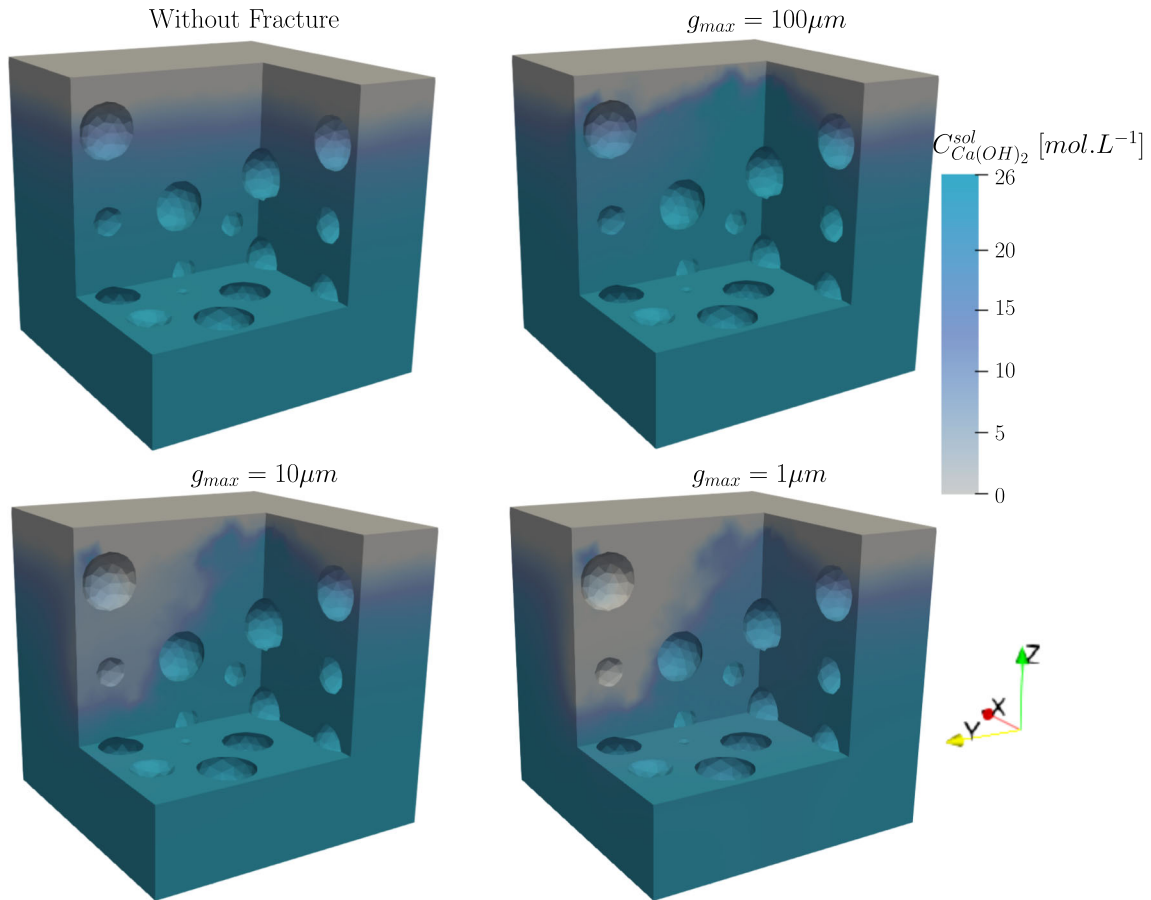

Fig. 12 Calcium leaching: portlandite field at 4600 days for the four critical gap values
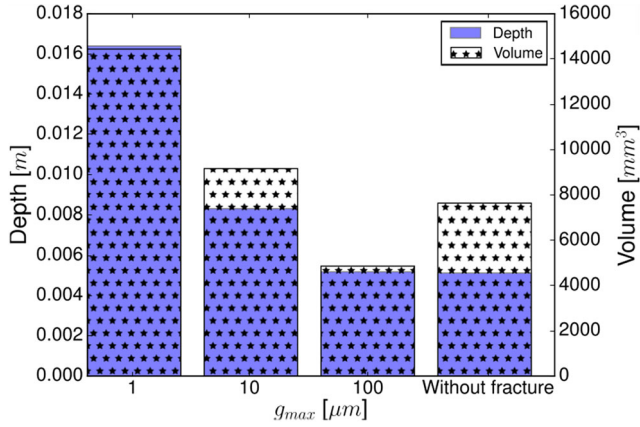
Fig. 13 Calcium leaching: evolution of the depth and the volume of portlandite dissolution with respect to the gap value at 4600 days

the species diffusion coefficient inside the discontinuity (see the differences between $g_{max} = 10\mu m$ and $g_{max} = 1\mu m$ in Fig. 12).

The crack opening is therefore a key parameter which has to be evaluated in geomaterial aging. Its local precise measurement is thus a new issue.

The Figs. 13 and 14 show the evolution of the portlandite depth and volume according to the critical gap value g_{max}. The depth corresponds to the zone in which the portlandite is totally dissolved. On one hand, the depth increases with the species diffusion coefficient inside the discontinuities. On the other hand, a localization effect is shown: the volume of dissolved portlandite for $g_{max} = 100\mu m$ is smaller than the one without discontinuity , nevertheless the depth is similar. As described in a recent paper [46], for a small fracture size, the discontinuity increases the material diffusivity and induces a preferential diffusion path, but its impact on the front of degradation (leaching) remains negligible. For a low diffusion kinetic, the solid reactions mainly buffer the degradation kinetics due to the strong difference between the solid concentration and the equilibrium aqueous value [46].
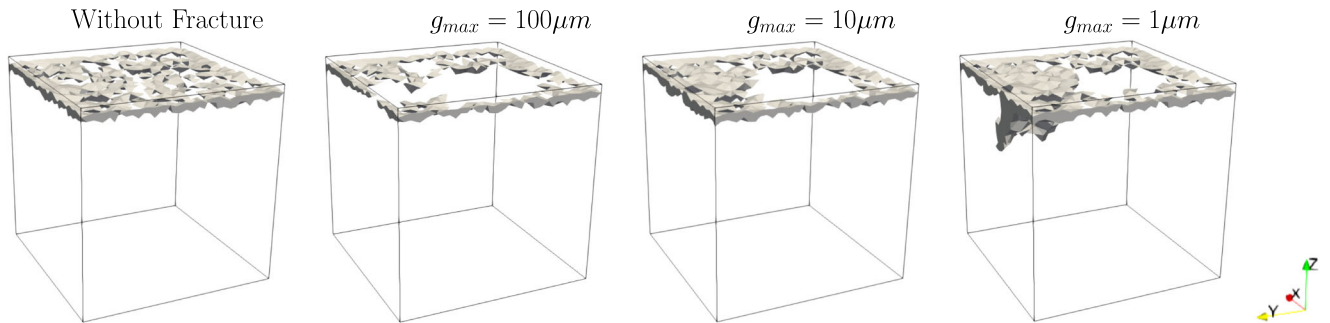
Table 8 Equilibrium table for the internal sulfate attack simulation: chemical reaction in the aggregates [6]

	Pyrite
OH^-	-1
SO_4^{2-}	1
Fe^{3+}	1
O_2	-3.75
$\log_{10}\left(K^{sol}\right)$	-246

Furthermore, the maximum depth does not correlate with the volume. These results highlight that numerical simulations of geomaterial aging are only accurate in 3D.

6.2 Internal Sulfate Attack

The Internal Sulfate Attack (ISA) is a chemical reaction between the sulfates released by the sulfate solid in the aggregates by oxidation process and the aluminates in the cement paste. This reaction induces the precipitation of ettringite in cement paste pores. The expansion of the ettringite can lead to the degradation of the material. We study the degradation of concrete due to the presence of iron sulfide in the aggregates. This kind of chemical degradation can affect dams [8, 40] and the dissolution of solid sulfate plays a major role in the issue of acid mine drainage [31].

We impose 10^{-7} $mol.L^{-1}$ of hydroxide concentration, 10^{-2} $mol.L^{-1}$ of dioxygen O_2 and a null concentration for the other species on the top boundary of the pre-cracked domain, Fig. 10a. We consider only the dissolution of the pyrite in the aggregates. The equilibrium constant are summarized in Tables 8 and 9. The initial concentration of pyrite is equal to 0.375 $mol.L^{-1}$, based on the simulations of [8].

The Fig. 15 shows the ettringite concentration field at 2500 days, about 7 years, for the four critical gap values. The ettringite and the iron(III) hydroxide precipitate preferentially around the aggregates due to the pyrite dissolution. As observed in the leaching study, the flow inside the discontinuities influences the diffusion. It

Fig. 14 Calcium leaching: portlandite dissolution areas at 4600 days for the four critical gap values

Table 9 Equilibrium table for the internal sulfate attack simulation: chemical reaction in the matrix [6]

	Portlandite	Ettringite	Katoite	$Fe(OH)_3$
Ca^{2+}	2	4	3	0
OH^-	1	6	4	3
$Al(OH)_4^-$	0	2	2	0
SO_4^{2-}	0	3	0	0
Fe^{3+}	0	0	0	1
$\log_{10}\left(K^{sol}\right)$	−5.19	−44.9	−20.5	−29.44

accelerates the O_2 diffusion inside the porous medium and the sulfate SO_4^{2-} diffusion from the aggregates to the porous medium. Furthermore, in this application, we observe that the size of the degraded zone increases with the critical gap.

The Fig. 16a shows the depth and the spatial average of the pyrite concentration in the aggregates denoted by $E(C_{Pyrite}^{sol}) = \frac{1}{N^{pt}} \sum_{i=0}^{N^{pt}} C_{Pyrite,i}^{sol}$ where N^{pt} is the

number of considered nodes. As expected, the depth increases with the flow inside the discontinuity except for the simulation $g_{\text{max}} = 100\mu m$.

The flow inside the discontinuities induces the localization of the O_2 even for small diffusion coefficients. However, the localization area is not in the vicinity of the aggregates which modifies the dissolution of the pyrite. Consequently, less aggregates are affected by the dissolution of pyrite without discontinuity than with discontinuity.

The Fig. 16a shows the spatial maximum and average of the ettringite concentration in the matrix with and without imposed SO_4^{2-} boundary conditions. As in the leaching study, we do not observe a link between the depth and the spatial average concentration. Although the ettringite precipitation is influenced by the discontinuities via the sulfate dissolution from the aggregate to the matrix, the maximum ettringite concentration does not seem to be influenced by the discontinuities. Furthermore, Fig. 16a highlights the impact of boundary conditions in the reactive transport behavior. Without imposed sulfate ions SO_4^{2-}, the
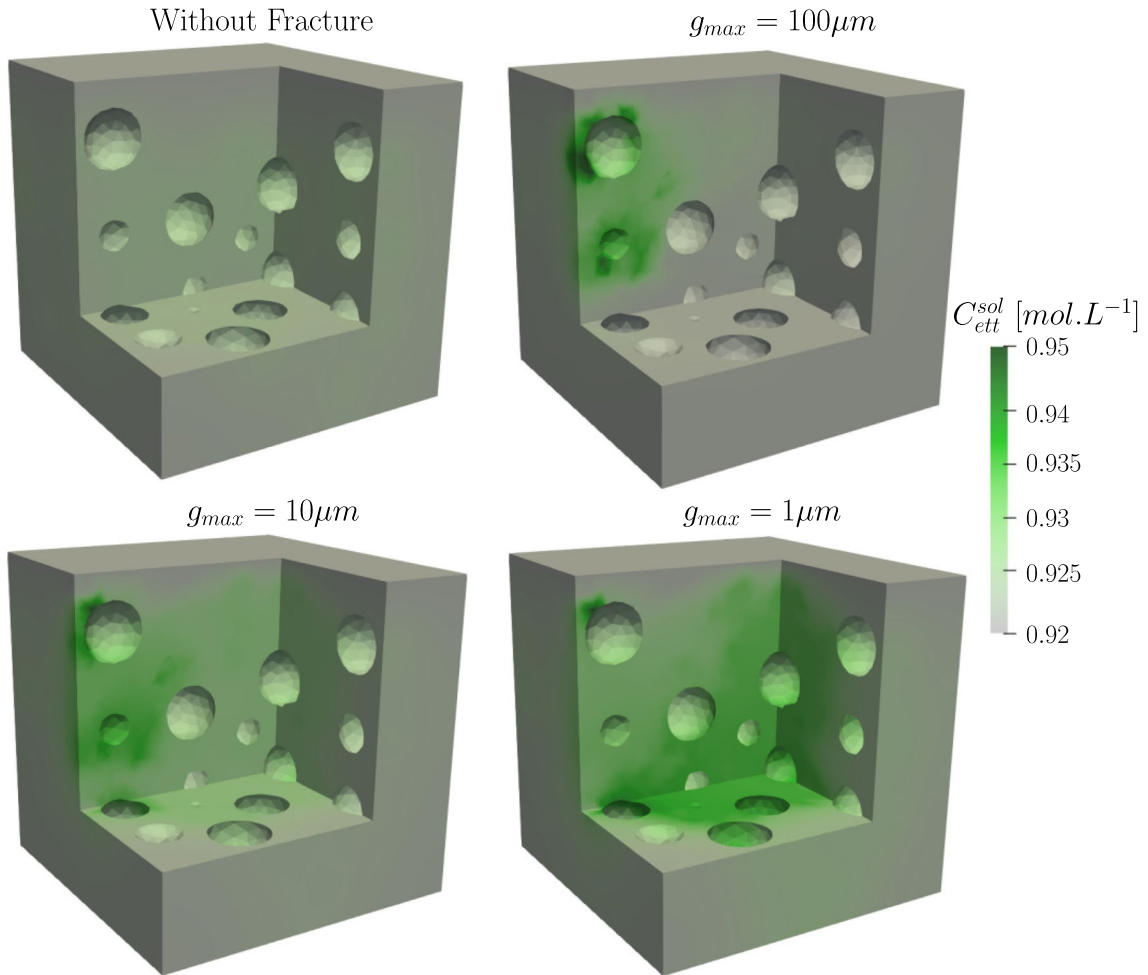

Fig. 15 Internal sulfate attack: ettringite field at 2500 days for the four critical gap values
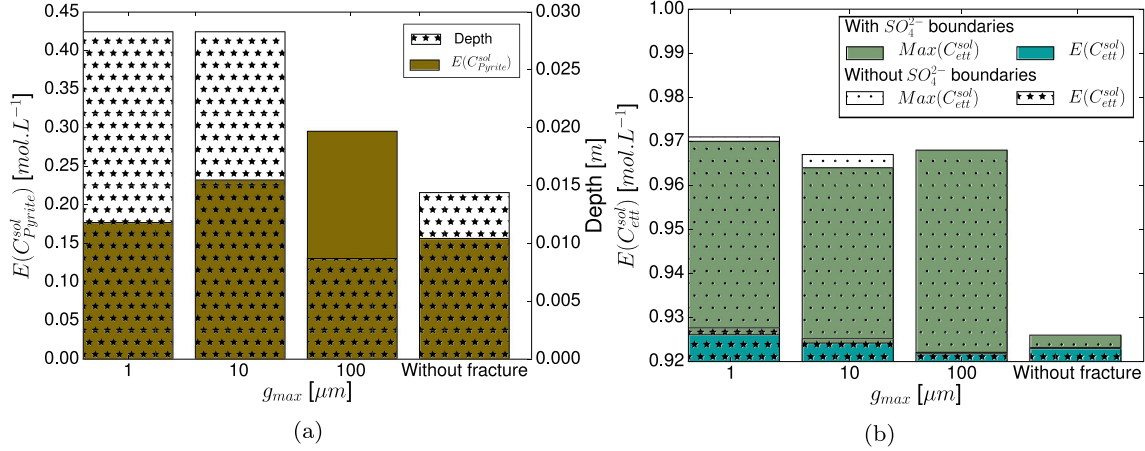
Fig. 16 Internal sulfate attack: **a** depth and spatial average of the pyrite concentration in the aggregates and **b** the spatial maximum and average of the ettringite concentration in the matrix with and without SO_4^{2-} boundary conditions

ettringite concentration increases. As a result, there is a competition between the ions leaching and the precipitation of the solid phases. The sulfate ions impact the reactive transport computing even though the concentration in the equilibrium with ettringite is around $10^{-6}\ mol.L^{-1}$. Nevertheless, the gap of spatial average concentration of ettringite is quite small. *As a first approach, a macroscopic model can only take into account the diffusion of O_2.* This assumption has been made in [8].

7 Concluding remarks

In this paper, a reactive transport model in discontinuous heterogeneous porous medium has been proposed and implemented in the IRSN XPER framework [47, 48]. The species transport across and along the discontinuities were taken into account in a multibody approach [45, 47]. Following [57], the discontinuous formulation was rested on the zero-thickness interface elements of the Goodman type. The geochemistry model was based on [10, 14] and allowed to solve a significant number of chemical reactions: aqueous reactions, sorption and solid precipitation and dissolution. Furthermore, to improve the chemical interaction modeling, the model has been extended with an electroneutrality condition. The strong coupling between the multibody approach and the reactive transport modeling allowed to model a large panel of chemical reactions in discontinuous-heterogeneous media, without the limitations of the introduction of interphases between matrix and inclusions or the necessity of a mesh refinement near the heterogeneities or the discontinuities.

The reactive transport is solved with a Sequential Non-Iterative Approach and an explicit to implicit time discretization. The geochemistry was assumed to be in local equilibrium assumption (static resolution). So, the chemical reactions were reversible and faster than species diffusion. The validity of the static assumption in the vicinity of the discontinuities must be verified. Note that a fine meshing, for example in the fracture, implies a small time step and, in this case, the Damköhler might not be strictly greater than 1. An outlook of this work can be a kinetic geochemistry model such as in [31].

To solve the diffusion problem, an analogy with the so-called thermal shock [44] was made and a time step criterion was proposed. The model was validated via a benchmark with the HYTEC software [64] for a porous medium without discontinuity.

The applications dealt with two kinds of chemical attacks in a pre-cracked concrete sample: Calcium leaching and Internal Sulfate Attack. The studies have highlighted two opposite effects of the discontinuities on the localization of the chemical degradation. First, the front of the degradation increases with the flow inside the discontinuities, and second, a safe area, with low impact on the chemical reaction, appears. Consequently, the depth is not sufficient to describe the degradation, more general 3D effects have to be taken into account.

In saturated porous media, the local diffusivity evolves linearly with the gap between each boundary of the discontinuity until a critical value [13, 19]. The diffusivity of the gap and the critical gap value impact the chemical degradation area and the kinetic of the reactive transport. The effective diffusion coefficient in the discontinuities was deduced from a partition of chloride diffusion fluxes between uncracked and crack domain [13]. A dedicated experiment with inverse analysis using a Finite Element computation can improve the local diffusion model. This

work has also underlined that precise in situ measurements of the crack opening is a key issue in predicting the aging of geomaterials.

Appendix 1: Mass action law for solid reaction

The law of mass action is rewritten with logarithmic unknowns in order to ensure the positivity of all concentrations.

$$\forall i \in [1, N^{sol}],$$
$$\xi_i^{sol}\left(\underline{C}^{aq}\right) = \left(K_i^{sol}\right)^{-1} \prod_{j=1}^{N^{aq,p}} \left(\gamma_j C_i^{aq,p}\right)^{S_{i,j}^{sol}} - 1 = 0$$
$$\xi_i^{sol}\left(\underline{C}^{aq}\right) =$$
$$\exp\left(-\ln\left(K_i^{sol}\right) + \sum_{j=1}^{N^{aq,p}} S_{i,j}^{sol}\left(\ln(\gamma_j) + \ln\left(C_i^{aq,p}\right)\right)\right) \tag{36}$$

The bijectivity of the exponential function induces:

$$\forall i \in [1, N^{sol}],$$
$$\xi_i^{sol*}\left(\underline{C}^{aq}\right) \stackrel{\text{def}}{=} \tag{37}$$
$$-\ln(K_i^s) + \sum_{j=1}^{N^{aq,p}} S_{i,j}^{sol}\left(\ln(\gamma_j) + \ln\left(C_i^{aq,p}\right)\right) = 0$$

Appendix 2: Jacobian terms of the geochemical numerical method

The chemical model reads (see Section 3):

find $\underline{C}^{aq,p} \in (\mathbb{R}_+^*)^{N^{aq}}, \underline{C}^{ad,p} \in (\mathbb{R}_+^*)^{N^{ad}}$ and $\underline{C}^{sol} \in (\mathbb{R}_+^*)^{N^{sol}}$ such that:

$$\begin{cases}
\underline{\Xi}^{aq} \stackrel{\text{def}}{=} \underline{C}_{tot}^{aq} - \left[\exp\left(\ln\left(\underline{C}^{aq,p}\right)\right) + \left(\underline{\underline{S}}^{aq}\right)^T \cdot \underline{C}^{aq,s}\right. \\
\qquad \left. + \left(\underline{\underline{S}}^{ad/aq}\right)^T \cdot C^{ad,s} + \left(\underline{\underline{S}}^{sol}\right)^T \cdot \underline{C}^{sol}\right] = \underline{0} \\
\underline{\Xi}^{ad} \stackrel{\text{def}}{=} \\
\underline{C}_{tot}^{ad} - \left[\exp(\ln(\underline{C}^{ad,p})) + \left(\underline{\underline{S}}^{ad/ad}\right)^T \cdot \underline{C}^{ad,s}\right] = \underline{0} \\
\underline{\Xi}^{sol} \stackrel{\text{def}}{=} \xi^{sol*}\left(\underline{C}^{aq,p}\right) = \underline{0} \\
\Xi^{el} \stackrel{\text{def}}{=} \sum_{i=1}^{N_p^{aq}+N_s^{aq}} z_i \exp\left(\ln\left(C_i^{aq}\right)\right) = 0
\end{cases} \tag{38}$$

The system is solved by a Newton-Raphson method. The Jacobian of this system is given by:

$$\underline{\underline{J}} \stackrel{\text{def}}{=} \begin{pmatrix} \frac{\partial \underline{\Xi}^{aq}}{\partial \ln(\underline{C}^{aq,p})} & \frac{\partial \underline{\Xi}^{aq}}{\partial \ln(\underline{C}^{ad,p})} & \frac{\partial \underline{\Xi}^{aq}}{\partial \underline{C}^{sol}} \\ \frac{\partial \underline{\Xi}^{ad}}{\partial \ln(\underline{C}^{aq,p})} & \frac{\partial \underline{\Xi}^{ad}}{\partial \ln(C^{ad,p})} & \underline{\underline{0}} \\ -\frac{\partial \underline{\Xi}^{sol}}{\partial \ln(\underline{C}^{aq,p})} & \underline{\underline{0}} & \underline{\underline{0}} \end{pmatrix} \tag{39}$$

where the Jacobian matrix terms are:

$$\begin{cases}
\frac{\partial \Xi_i^{aq}}{\partial \ln(C_j^{aq,p})} = \\
-\delta_{i,j}\exp(\ln(C_i^{aq,p})) - \sum_{k=1}^{N_s^{aq}} S_{j,k}^{aq} \frac{\partial C_i^{aq,s}}{\partial \ln(C_j^{aq,p})} \\
\qquad - \sum_{k=1}^{N_s^{ad}} S_{j,k}^{ad} \frac{\partial C_k^{ad,s}}{\partial \ln(C_j^{aq,p})} \\
\frac{\partial \Xi_i^{aq}}{\partial \ln(C_j^{ad,p})} = -\sum_{k=1}^{N_s^{ad}} S_{j,k}^{ad} \frac{\partial C_k^{ad,s}}{\partial \ln(C_j^{ad,p})} \\
\frac{\partial \underline{\Xi}_i^{ad}}{\partial \ln(C_i^{aq,p})} = -\sum_{k=1}^{N_s^{ad}} S_{i,k}^{ad/ad} \frac{\partial C_k^{ad,s}}{\partial \ln(C_j^{aq,p})} \\
\frac{\partial \underline{\Xi}_i^{ad}}{\partial \ln(C_j^{ad,p})} = \\
-\delta_{i,j}\exp(\ln(C_i)) - \sum_{k=1}^{N_s^{ad}} S_{i,k}^{ad/ad} \frac{\partial C_k^{ad,s}}{\partial \ln(C_j^{ad,p})} \\
\frac{\partial \underline{\Xi}_i^{sol}}{\partial \ln(C_j^{aq,p})} = \\
-\sum_{k=1}^{N_p^{ad}} S_{i,k}^{sol}\left(\frac{\partial \ln(\gamma_k)}{\partial \ln(C_j^{aq,p})} + \delta_{k,j}\ln(C_k^{aq,p})\right) \\
\frac{\partial \Xi_i^{aq}}{\partial C_j^{sol}} = -\sum_{k=1}^{N^{sol}} S_{j,k}^{sol}\delta_{k,j}
\end{cases} \tag{40}$$

with :

$$\begin{cases}
\frac{\partial C_i^{aq,s}}{\partial \ln(C_j^{aq,p})} = \left(-\frac{\partial \ln(\gamma_i)}{\partial \ln(C_i^{aq,p})} + \sum_{k=1}^{N_p^{aq}} S_{i,k}^{aq}\left(\frac{\partial \ln(\gamma_k)}{\partial \ln(C_j^{aq,p})}\right.\right. \\
\qquad \left.\left. +\delta_{k,j}\ln(C_k^{aq,p})\right)\right) C_i^{aq,s} \\
\frac{\partial C_i^{ad,s}}{\partial \ln(C_j^{aq,p})} = \left(\sum_{k=1}^{N_p^{aq}} S_{i,k}^{ad/aq}\left(\frac{\partial \ln(\gamma_k)}{\partial \ln(C_j^{aq,p})}\right.\right. \\
\qquad \left.\left. +\delta_{k,j}\ln\left(C_k^{aq,p}\right)\right)\right) C_i^{ad,s} \\
\frac{\partial C_i^{ad,s}}{\partial \ln(C_j^{ad,p})} = \left(\sum_{k=1}^{N_p^{ad}} S_{i,k}^{ad/ad}\delta_{k,j}\ln(C_k^{ad,p})\right) C_i^{ad,s} \\
\frac{\partial \ln(\gamma_i)}{\partial \ln(C_j^{aq,p})} = -Az_i^2\left(\frac{1}{2\sqrt{IS}\left(1+\sqrt{IS}\right)^2} - b\right) \\
\qquad \times \delta_{i,j}z_j^2\exp(\ln(C_j^{aq,p}))
\end{cases} \tag{41}$$

If the electroneutrality is imposed (26), the chemical system is overdetermined. As implemented in CHESS software [63], one mass conservation relations of the aqueous species is replaced by the electroneutrality equation. The associated Jacobian term is:

$$\frac{\partial \Xi^{el}}{\partial \ln(C_i^{aq})} = z_i \exp(\ln(C_i^{aq})) \ \forall i \in [1, N^{aq-1}] \qquad (42)$$

Declarations

Conflict of Interests The authors declare that they have no conflict of interest.

References

1. Amir, L., Kern, M.: A newton–krylov method for coupling transport with chemistry in porous media
2. Archie, G.E.: The electrical resistivity log as an aid in determining some reservoir characteristics trans. AIME **146**(01), 54–62 (1942)
3. Bergheau, J.-M., Leblond, J.-B.: Implémentation numérique et application de modèles de diffusion/réaction dans les solides. 14ème Colloque National en Calcul des Structures (2019)
4. Bichet, L.: Mécanisme de transport dans la fissuration des matériaux hétérogenes : application a la durée de vie d'éxploitation des centrales nucléaires. PhD thesis, Université de Montpellier II (2017)
5. Hilaire, A.: Etude des déformations différées des bétons en compression et en traction, du jeune au long terme : application aux enceintes de confinement. PhD thesis, Ecole Normale Supérieure de Cachan (2014)
6. Blanc, P.h., Lassin, A., Piantone, P., Azaroual, A., Jacquemet, N., Fabbri, A., Gaucher, E.C.: Thermoddem: A geochemical database focused on low temperature water/rock interactions and waste materials. Appl. Geochem. **27**(10), 2107–2116 (2012)
7. Budiansky, B., OĆonnel, R.J.: Elastic moduli of a cracked solid. Int. J. Solids Struct. **12**, 81–97 (1976)
8. Campos, A., López, C.M., Aguado, A.: Diffusion reaction model for the internal sulfate attack in concrete. Constr. Build. Mater. **102**, 531–540 (2016)
9. Carrayrou, J., Hoffmann, J., Knabner, P., Kräutle, S., De Dieuleveult, J., Erhel, C., Van Der Lee, J., Lagneau, V., Mayer, K.U., MacQuarrie, K.T.B.: Comparison of numerical methods for simulating strongly nonlinear and heterogeneous reactive transport problems the MoMaS benchmark case. Comput. Geosci. **14**, 483–502 (2010)
10. De Dieuleveult, C., Erhel, J., Kern, M.: A global strategy for solving reactive transport equations. J. Comput. Phys. **228**, 6395–6410 (2009)
11. De Windt, L., Bradreddine, R., Lagneau, V.: Long-term reactive transport modelling of stabilized/solidified waste: from dynamic leaching tests to disposal scenarios. J. of Hazard. Mater. **139**, 529–536 (2007)
12. Delaume, E.: Méthode de raffinement local adaptatif multiniveaux pour la fissuration des matériaux hétérogènes. PhD thesis, Université Montpellier II (2017)
13. Djerbi, A., Bonnet, S., Khelidj, A., Baroghel-Bouny, V.: Influence of traversing crack on chloride diffusion into concrete. Cem. Conc. Res. **38**, 877–883 (2008)
14. Erhel, J., Sabit, S., De Dieuleveult, C.: Developments in parallel, distributed, grid and cloud computing for engineering. In: Topping, B.H.V., Iványi, P. (eds.) UK, Chapter 7: Solving Partial Differential Algebraic Equations and Reactive Transport Models, pp. 151–169 (2013)
15. Erhel, J., Migot, T.: Characterizations of solutions in geochemistry: existence, uniqueness, and precipitation diagram. Comput. Geosci. **23**, 523–535 (2019)
16. Haas, J., Nonat, A.: From csh to cash: Experimental study and thermodynamic modelling. Cem. Conc. Res. **68**, 124–138 (2015)
17. Heukamp, F.H.: Chemomechanics of Calcium Leaching of Cement-Based Materials at Different Scales: The Role of CH-Dissolution and C-S-H-Degradation on Strength and Durability Performance of Materials and Structures. PhD thesis, Massachussetts Institute of Technology (2003)
18. Idiart, A.E., Bisschop, J., Caballero, A., Lura, P.: A numerical and experimental study of aggregate-induced shinkrage craking in cementitious composites. Cem. Conc. Res. **42**, 272–281 (2012)
19. Idiart, A.E., López, C.M., Carol, I.: Chemo-mechanical analysis of concrete cracking and degradation due to external sulfate attack: A meso-scale model. Cem. Concr. Compos. **33**, 411–423 (2011)
20. Jebli, M., Jamin, F., Garcia-Diaz, E., El Omari, M., El Youssoufi, M.S.: Influence of leaching on the local mechanical properties of an aggregate-cement paste composite. Cem. Concr. Compos. **73**, 241–250 (2016)
21. Kchakech, B.: Etude de l'influence de l'échauffement subi par un béton sur le risque d'expansions associées à la Réaction Sulfatique Interne. PhD thesis, Université Paris-Est (2016)
22. Kondo, D., Dormieux, L.: Approche micromécanique du couplage perméabilité-endommagement. Compte Rendu Mecanique (2004)
23. Lagneau, V., Van Der Lee, J.: Hytec results of the momas reactive transport benchmark. Comput. Geosci. **14**, 435–449 (2010)
24. Lagneau, V., Van Der Lee, J.: Operator-splitting-based reactive transport models in strong feedback of porosity change: The contribution of analytical solutions for accuracy validation and estimator improvement. J. Contam. Hydrol. **112**, 118–129 (2010)
25. Leblond, J.B., Bergheau, J.M., Lacroix, R., Huin, D.: Implementation and application of some nonlinear models of diffusion/reaction in solids. Finite Elements in Anal. Des. **132**, 8–26 (2017)
26. Liaudat, J.: Experimental and numerical study of the effect of stress on ASR expansions in concrete. PhD thesis, School of Civil Engineering of Barcelona (2018)
27. Lothenbach, B., Kulik, D., Matschei, T., Balonis, M., Baquerizo, L., Dilnesa, B.Z., Miron, D.G., Myers, R.: Cemdata18: A chemical thermodynamic database for hydrated portland cements and alkaliactivated materials. Cem. Conc. Res. **115**, 472–506 (2019)
28. Marquié, C., Dauzeres, A., Richard, B., Nahas, G.: Concrete aging in containment building and deep geological disposal facilities: the ODOBA project. Transactions, SMiRT-25 Charlotte, NC, USA (2019)
29. Martin, R.P., Metalssi, O.O., Toutlemonde, F.: Importance of considering the coupling between transfer properties, alkali leaching and expansion in the modelling of concrete beams affected by internal swelling reactions. Constr. Build. Mater. **49**, 23–30 (2013)
30. Mayer, K.U.: A Numerical Model for Multicomponent Reactive Transport in Variability Saturated Porous Media. PhD thesis, University of Waterloo (1999)
31. Mayer, K.U., Frind, E.O., Blowes, D.W.: Multicomponent reactive transport modeling in variably saturated porous media using a generalized formulation for kinetically controlled reactions. Water Resour. Res. **38**(9), 1–21 (2002)
32. Mayer, K.U., MacQuarrie, K.T.B.: Solution of the MoMaS reactive transport benchmark with MIN3P—model formulation and simulation results. Comput. Geosci. **14**, 405–419 (2010)

33. Michel, J.C., Suquet, P., Thébaud, F.: Une modélisation du rôle des interfaces dans le comportement des composites à matrice métallique. Revue Europé,enne des Éléments **3**(4), 573–595 (1994)

34. Miura, T., Maruyama, I., Nakamura, H., Yammoto, Y.: Feedback system of ion transfer through cracks during deterioration of mortar due to sulfate attack evaluated by rbsm-truss network model. J. of Adv. Concr. Tech. **15**, 610–626 (2017)

35. Morel, F., Morgan, J.: A numerical method for computing equilibria in aqueous chemical systems. Environ. Sci. Tech. **6**(1), 58–67 (1972)

36. Nardi, A., Idiart, A., Trichero, P., Manuel, L., de Vries, L.M., Molinero, J.: Interface comsol-phreeqc (icp), an efficient numerical framework for the solution of coupled multiphysics and geochemistry. Computer Geosci. **69**, 10–21 (2014)

37. Neji, M., Bary, B., Le Bescop, P., Burlion, N.: Swelling behavior of ion exchange resins incorporated in tri-calcium silicate cement matrix: I. chemical analysis. J. Nucl. Mater. **467**, 544–556 (2015)

38. Nilenius, F., Larsson, F., Lundgren, K., Runesson, K.: Mesoscale modelling of crack-induced diffusivity in concrete. Comput. Mech. **55**(2), 359–370 (2015)

39. Ochs, M., Mallants, D., Wang, L.: Radionuclide and Metal Sorption on Cement and Concrete. Chapter 2: Cementitious Materials and Their Sorption Properties. Springer International Publishing, Berlin (2016)

40. Oliveira, I., Cavalaro, H.P., Aguado, A.: New kinetic model to quantify the internal sulfate attack in concrete. Cem. Conc. Res. **43**, 95–104 (2013)

41. Ollivier, J.P., Vichot, A.V., Capmas, A., Nonat, A., Torrenti, J.-M., Damidot, D., Le Bescop, P., Pons, G., Guérinet, M., Acker, P., Guiraud, P., Rougeau, P., Baroghel-Bouny, V., Cussigh, F., Laurens, S., Gagné, R., Capra, B., Linger, L., Carles-Gibergues, A., Honain, H., Escadeillas, G., Colina, H., Robert, F., Debicki, G., Fryda, H., Saucier, F., Lamberet, S., Scrivener, K., Guinot, D., Sommain, D.: La durabilité des bétons. Presses de l'Ecole Nationale des Ponts et Chaussées (2008)

42. Papachristos, E., Scholtès, L., Donzé, V., Chapeyre, B.: Intensity and volumetric characterizations of hydraulically driven fractures by hydro-mechanical simulations. Int. J. Rock Mech. Min. Sci. **93**, 163–178 (2017)

43. Parkhurst, D.L., Wissmeier, L.: Phreeqcrm: A reaction module for transport simulators based on the geochemical model phreeqc. Adv. Water Resour. **8**, 176–189 (2015)

44. Pelissou, C.: Discrétisation spatiotemporelle du problème thermique à deux champs : application au procédé de forgeage à chaud. PhD thesis, École Nationale Supérieure des Mines de Paris (2005)

45. Perales, F., Bourgeois, S., Chrysochoos, A., Monerie, Y.: Two field multibody method for periodic homogenization in fracture mechanics of non linear heterogeneous materials. Eng. Fracture Mech. **75**, 3378-3398 (2008)

46. Perko, J., Ukrainczyk, N., Savija, B., Phung, Q.T., Koenders, E.A.B.: Influence of Micro-Pore Connectivity and Micro-Fractures on Calcium Leaching of Cement Pastes—A Coupled Simulation Approach Mat 13 (2697)

47. Perales, F., Dubois, F., Monerie, Y., Piar, B., Stainier, L.: A nonsmooth contact dynamics-based multi-domain solver. code coupling (xper) and application to fracture. Eu. J. Comput. Mech. **19**(4), 389–417 (2010)

48. Perales, F., Dubois, F., Monerie, Y., Mozul, R., Babik, F.: Xper : une plateforme pour la simulation numérique distribuée d'interactions multiphysiques entre corps 14ème Colloque National en Calcul des Structures (2019)

49. J Perko, K.U., Mayer, G., Kosakowski, L., De Windt, J., Govaerts, D., Jacques, D.S.u., Meeussen, J.C.L.: Decalcification of cracked cement structure. Comput. Geosci. **19**, 673–693 (2015)

50. Perko, J., Seetharam, S., Mallants, D.: Verification and validation of flow and transport in cracked saturated porous media. Excerpt from the Proceedings of the 2011 COMSOL Conference in Stuttgart (2011)

51. Planel, D., Sercombe, J., Le Bescop, P., Adenot, F., Torrenti, J.-M.: Long-term performance of cement paste during combined calcium leaching-suflate attack: kinetics and size effect. Cem. Conc. Res. **36**, 137–143 (2006)

52. Poyet, S., Sellier, A., Capra, B., Foray, G., Torrenti, J.-M., Cognon, E., Bourdarot, E.: Chemical modelling of alkali silica reaction: Influence of the reactive aggregate size distribution. Mater. Struct. **40**, 229–239 (2007)

53. Repina, M., Bouyer, F., Lagneau, V.: Reactive transport modeling of glass alteration in a fractured vitrified nuclear glass canister: From upscaling to experimental validation. J. Nucl. Mater. **528**, 151869 (2020)

54. Salgues, M., Sellier, A., Multon, S., Bourdarot, E., Grimal, E.: DEF modelling based on thermodynamic equilibria and ionic transfers for structural analysis. Eur. J. Environ. Civ. Eng. **18**(4), 1–26 (2014)

55. Samson, E., Marchand, J.: Modeling the transport of ions in unsaturated cement-based materials. Comput. Struct. **85**, 1740–1756 (2007)

56. Savija, B., Pacheco, J., Schlangen, E.: Lattice modeling of chloride diffusion in sound and cracked concrete. Cem. Conc. Compos. **42**, 30–40 (2013)

57. Segura, J.M., Carol, I.: On zero-thickness interface elements for diffusion problems. Int. J. Numer. Anal. Methods Geomech. **28**(9), 947–62 (2004)

58. Sellier, A., Multon, S.: Chemical modelling of delayed ettringite formation for assessment of affected concrete structures. Cem. Conc. Res. **108**, 72–86 (2018)

59. Socié, A.: Modélisation chimiomécanique de la fissuration de matériaux cimentaires : vieillissement et tenue des enceintes de confinement des centrales nucléaires. PhD thesis, Université de Montpellier (2019)

60. Steefel, C.I., Lasaga, A.C.: A coupled model for transport of multiple chemical species and kinetic precipitation/dissolution reactions with application to reactive flow in single phase hydrothermal systems. Am. J. Sci. **294**, 529–592 (1994)

61. Stora, E., Bary, B., He, Q.-C., Deville, E., Montarnal, P.: Modelling and simulations of the chemo-mechanical behaviour of leached cement-based materials leaching process and induced loss of stiffness. Cem. Conc. Res. **39**, 763–772 (2009)

62. Suquet, P.M.: CSIM Courses and lectures - No. 302. International center for mechanical sciences. Chapter "Discontinuities and Plasticity" in Non Smooth Mechanics and Applications (1988)

63. Van der Lee, J.: Thermodynamic and mathematical concepts of CHESS. Ecole Nationale Supérieure des Mines de Paris (2009)

64. Van Der Lee, J., De Windt, L., Lagneau, V., Goble, P.: Module-oriented modeling of reactive transport with HYTEC. Comput. Geosci. (2003)

65. Wu, T., Wrigger, P.: Multiscale diffusion-thermal-mechanical cohesive zone model for concrete. Computer Mech. **55**, 999–1016 (2015)